

Towards a Double Tip Vacuum Fiber Microscope

Florian Matthias Giefer

Bachelorarbeit in Physik
angefertigt im Institut für Angewandte Physik

vorgelegt der
Mathematisch-Naturwissenschaftlichen Fakultät
der
Rheinischen Friedrich-Wilhelms-Universität
Bonn

August 2022

Ich versichere, dass ich diese Arbeit selbstständig verfasst und keine anderen als die angegebenen Quellen und Hilfsmittel benutzt sowie die Zitate kenntlich gemacht habe.

Bonn,
Datum

.....
Unterschrift

- 1. Gutachter: Prof. Dr. Sebastian Hofferberth
- 2. Gutachter: Prof. Dr. Dieter Meschede

Acknowledgements

First and foremost, I would like to thank Dr. Hannes Pfeifer and Lukas Tenbrake for their inexhaustible guidance regarding this thesis, as well as Prof. Dr. Sebastian Hofferberth for the great chance to work on such an interesting project with so many great people. A big thank you also belongs to all the other members of our group for their great answers to my minor and sometimes extensive questions, as well as for their support with various problems. Then I want to thank Professor Meschede for offering to be my second examiner. I also want to thank Jasper and Lukas for letting me use some of their measurement and evaluation software and send a special thank you to my proofreaders: Maria, Judith and, of course, Lukas and Hannes. Last but not least, I want to thank my family and friends for their ongoing encouragement and great interest in my work. Thank you so much!

Contents

1	Introduction	1
2	Foundational Knowledge	2
2.1	Fiber-Fabry-Perot Cavities	2
2.1.1	Introduction to Fabry-Perot Cavities	2
2.1.2	Fiber Cavities	3
2.2	Cavity Optomechanics with Polymer Structures	5
2.2.1	Cavity Optomechanics Basics	5
2.2.2	Membrane in the Middle Optomechanical Systems	5
2.2.3	Fabrication of Polymer Resonators	5
2.3	Optomechanical Measurements and Cavity Locks	6
3	Building the Vacuum Fiber Microscope	7
3.1	Motivation for the Experiment	7
3.2	Project Draft and Experimental Demands	8
3.3	Construction	9
3.3.1	Structural Construction	9
3.3.2	Mechanical and Electrical Construction	11
3.4	Coding a Control Software	19
3.5	Building Fiber Holders	19
3.6	Integration into Vacuum System	24
3.6.1	Building the Vacuum System	24
3.6.2	Constructing a Transport for Introduction to Vacuum	27
3.6.3	Moving the Experiment into the Vacuum Chamber	27
3.7	Efforts to Stabilize the Cavity	30
3.8	Future Extensions	30
4	First Measurements and Optimizations	32
4.1	Finesse Measurement Procedure	32
4.1.1	Measurements of Fiber Candidates	35
4.1.2	Characterization of the Mirror Alignment	38
4.2	Polymer Drum Resonance Measurement	40
5	Summary and Outlook	43
A	Raw Data	45
A.1	Data of fiber candidates	45

A.2 Data: Characterization of the mirror alignment	46
A.2.1 Translation over mirror substrate	46
A.2.2 Rotation over mirror substrate	50
Bibliography	53
List of Figures	56
List of Tables	60

Introduction

Around 2000 B.C. the Egyptians created metallic mirrors, some of the first optical devices in history. The Greeks methodized the subject over 1000 years later by various early theories about the nature of light [1] thus kick starting optics as a field of science in the process. Johannes Keppler noticed one of the first optomechanical effects during his study of comets in 1619. He realized that the tails of comets always face away from the sun and so discovered the effect of radiation pressure, showing that light can have a mechanical impact [2][3]. It would take another 350 years for the field of cavity optomechanics to emerge, as it first became significant through considerations in gravitational wave astronomy in the 1970s because the radiation pressure of individual photons of the lasers, used in the interferometers for gravitational wave research, can lead to a tiny amount of mirror shaking and therefore can be a limiting factor for the interferometers precision. Some pioneering optomechanics work at the time was conducted by Vladimir Braginsky [3]. Fast forwarding another 50 years, today cavity optomechanics is a vivid field of research, offering rich possibilities in future developments for telecommunication technologies and sensor construction, for example by providing optomechanical alternatives to surface acoustic wave filters and micro electronic mechanical systems, but also paving the way for advances in quantum computing and quantum many body dynamics research (see also Sec. 5).

A recent development made by Mader, Reichel, Hänsch and Hunger is of special interest for this thesis. In their paper “A scanning cavity microscope” [4] they showed that it is possible to build cavities with scannable length between a fiber mirror and a mirror substrate, and to then do surface scans over the substrate. The setup in this thesis is inspired by this paper and aims to be a similar structure in vacuum that can, instead of imaging gold nanoparticles as they did, investigate small polymer oscillators and even, by utilizing not one but two fiber mirrors simultaneously, characterize arrays of coupled polymer resonators. Because of the similarities this paper also inspired the title of this thesis, even though no literal microscope, in the narrowest sense, is built.

Foundational Knowledge

2.1 Fiber-Fabry-Perot Cavities

2.1.1 Introduction to Fabry-Perot Cavities

A Fabry-Perot resonator is made of two opposing mirrors facing each other. At least one mirror is sufficiently transmittive and so light can enter the cavity. As light enters, it then reflects back and forth between the two mirror surfaces and so, if the light wave interferes constructively with itself after one circulation, a strong field builds up inside of the cavity as more and more power enters. This field keeps increasing until a balance with the light lost from the cavity is reached, for example by misalignment, scattering, absorption or transmission through the mirror. Fabry-Perot cavities are an important basic concept in optics and explained in detail in most standard textbooks, the explanation here will go alongside [5, p. 196-202], where further explanations can also be found. Now consider two light rays that enter the cavity at an angle θ , their phase shift can be formulated as

$$\delta = k \cdot l_{\text{opt}} = 2nkl \cos(\theta) \quad (2.1)$$

with n the reflective index of the material, $k = \frac{2\pi}{\lambda}$ the angular wave number, l the length of the cavity and l_{opt} the optical path length. This phase shift has to equal $N \cdot 2\pi$ for constructive interference to occur. To determine the transmitted electric field one can consider all individual transmitted rays and sum their contribution in an geometric series:

$$E_{\text{tr}} = \sqrt{T'T}E_{\text{in}} + \sqrt{RR'}e^{i\delta}\sqrt{TT'}E_{\text{in}} + RR'e^{2i\delta}\sqrt{TT'}E_{\text{in}} + \dots = \frac{\sqrt{TT'}E_{\text{in}}}{1 - \sqrt{RR'}e^{i\delta}} \quad (2.2)$$

With T , T' and R , R' the transmission- and reflection coefficients of the first and second mirror respectively, E_{tr} the transmitted electric field and E_{in} the incoming electric field.

Equation 2.1 shows that there exists a periodic transmission spectrum. The Frequency distance between two neighboring transmission lines is called the “Free Spectral Range”, in short “FSR”. It can be calculated as:

$$\delta\nu_{\text{FSR}} = \nu_{N+1} - \nu_N = \frac{c}{2nl} \quad (2.3)$$

where N numerates the maxima. If one now considers the resolution capabilities of the cavity, one

notices that it is limited by possible mutual obscuration among the resonance peaks. A measure for the broadness of the transmission lines is the so called “full width at half maximum” or in short “FWHM”, it can be calculated as the difference between the two points at half height of a peak $\Delta\nu_{\text{FWHM}} = \nu_1 - \nu_2$. The quotient of free spectral range and full width at half maximum of the peak is now a measure for the resolution capabilities and is called the “finesse”.

$$F = \frac{\delta\nu_{\text{FSR}}}{\Delta\nu_{\text{FWHM}}} \quad (2.4)$$

This is also a measure for how often the light is reflected back and forth in the cavity before eventually being lost. A clarification of the concepts of FSR and FWHM is visible in Fig. 2.1

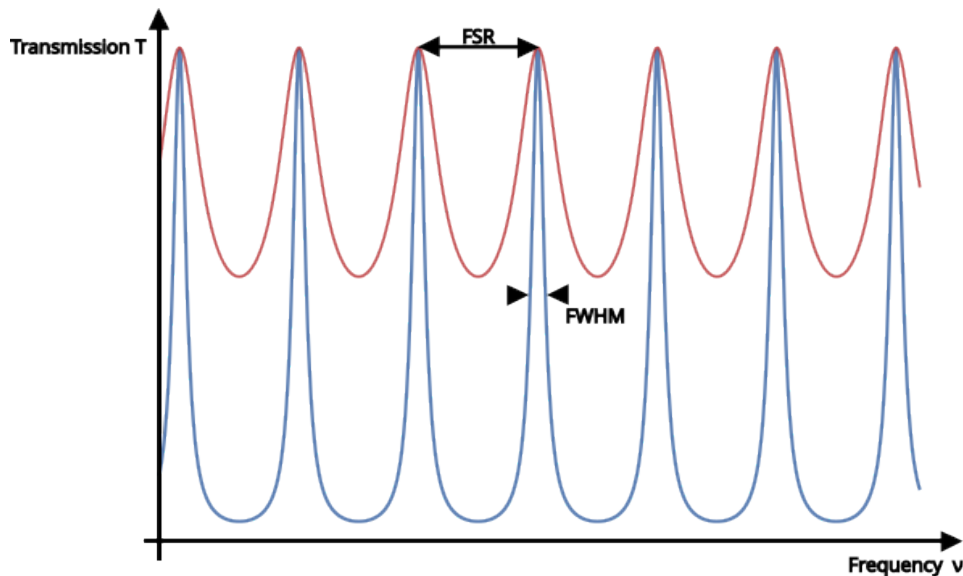


Figure 2.1: Qualitative plot of the transmission spectrum into the cavity for a lower (red) and a higher finesse (blue).

2.1.2 Fiber Cavities

Bragg Reflectors

A Bragg Reflector is a wavelength dependent mirror that consists of thin alternating material sheets with alternating refractive indices, most of the time dielectrics are used to minimize absorption. At every interface a part of the incoming light is reflected, at the same time the thicknesses and refractive indices of the two alternating materials are tweaked to create destructive interference between the transmitted rays by introducing a phase shift of 180° and thus increasing the reflection which is constructively interfering. For this to work one ideally wants to create material thicknesses that lead to an optical path length, quarter the target wavelength, so a phase shift of 180° is collected by a ray reflected of the second interface compared to the incoming ray. To make the reflection more spectrally broadband, the sheet thicknesses are often varied along the Bragg stack, so that for every desired wavelength the phase condition is fulfilled precisely enough somewhere down the stack. Further information on Bragg

reflectors can be found in [6, p. 555-559].

Fiber Mirrors

The fiber mirrors used in this experiment are manufactured in a cooperation with the research groups of Professor Linden and Professor Köhl. They consist of raw optical fibers that get cleaved at their tips and then shot at by a powerful CO₂-Laser (Fig. 2.2) at $\lambda = 9.3 \mu\text{m}$ which lies within an absorption peak of silica glass, due to Si–O–Si resonance vibration modes [7]. Radially symmetric Gaussian beam pulses are applied to the surface and thus a carve out of Gaussian geometry is created, which approximates a spherical/parabolic mirror surface [8, p. 12-13]. This geometry is advantageous compared to a flat one, as it concentrates the light rays towards the optical axis and thus allows for lower losses and easier cavity alignment. This fiber tip is then sent off to a company, specialized for optical coatings, to create a Bragg reflector on the surface by alternating application of Ta₂O₅ ($n_1(780 \text{ nm}) = 2.0738$ [9]) and SiO₂ ($n_2(780 \text{ nm}) = 1.4610$ [10]) layers to form a finished fiber mirror that is capable to reach a reflectiveness of 99.99 % in the wavelength range of about 770 – 820 nm where we operate at [8, p. 12-13] (Note that $\sqrt{n_1} \approx n_2$, a rule of thumb for good destructive interference of the transmitted rays).

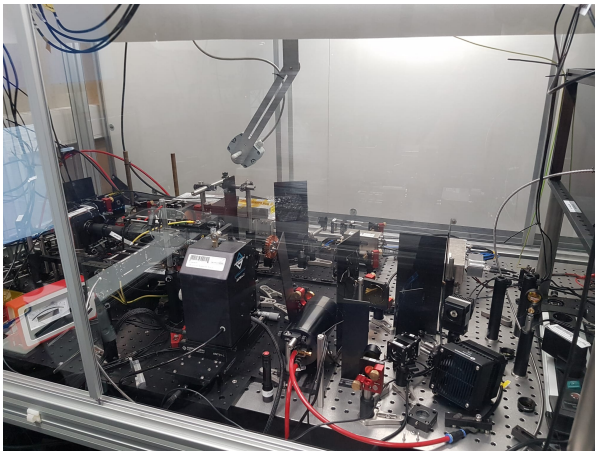


Figure 2.2: The fiber shooting setup.

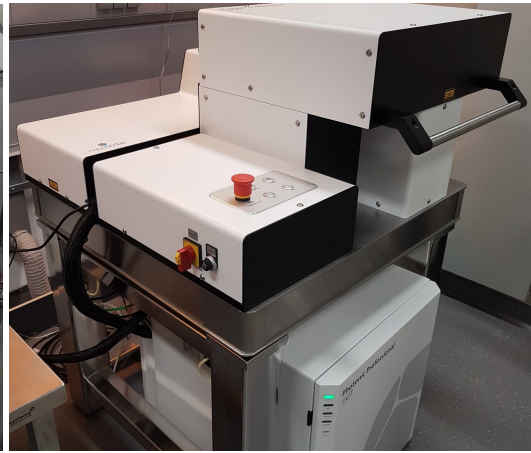


Figure 2.3: The Nanoscribe 3D-Printing system.

Particularities with Fiber Cavities

A very interesting part about fiber mirrors is their Gaussian geometry. Near the center of the fiber mirror this is a good approximation of a spherical/parabolic geometry, but further outwards the deviation gets substantial. This leads to additional clipping losses if the cavity mode is large enough, which will then lead to a finesse decrease. The cavity mode size increases with cavity length, thus one expects a rather constant finesse for small cavity lengths and a decrease as soon as clipping losses begin to play a role. A more detailed explanation of this effect can be found in [11, p. 20-22].

A further effect emerges through the fact that the cavity is fiber coupled. Because of the mode filtering inside the fiber core interference between the light reflected at the incoupling fiber mirror back into the fiber and the light that leaves the cavity through the incoupling fiber arises. Through that the back reflection line shape of fiber Fabry-Perot cavities consists of a normal Lorentzian and an additional

dispersive part. As the non incoupling fiber does not provide any directly reflected light to interfere with, the transmission spectrum has just a Lorentzian form. This is explained in full detail in [11, p. 24-31].

2.2 Cavity Optomechanics with Polymer Structures

2.2.1 Cavity Optomechanics Basics

A cavity optomechanical system has a coupling between a radiation mode of the cavity and a displacement of an mechanical oscillator \hat{x} . Therefore the frequency of the radiation mode can be written in dependence of \hat{x} as $\omega_{\text{opt}}(\hat{x})$. A Taylor expansion leads to the basic cavity-optomechanical Hamiltonian [12, p. 5-6]

$$\hat{H}_0 = \hbar \left(\omega_{\text{opt}}(0) - G\hat{x} \right) \hat{a}^\dagger \hat{a} + \hbar \Omega_M \hat{b}^\dagger \hat{b} + \dots \quad (2.5)$$

The Hamiltonian states that the total energy of the cavity optomechanical system is approximately composed of the sum of the energy in the cavity mode and the energy of the mechanical mode, as $\hat{a}^\dagger \hat{a}$ denotes the number of photons inside the optical cavity mode and $\hat{b}^\dagger \hat{b}$ is the number of phonons inside of the mechanical mode. Ω_M is the mechanical frequency, the coupling constant G also called the “frequency pull parameter” denotes the optomechanical frequency shift per displacement [12, p. 5-6]. This Hamiltonian describes many optomechanical systems, starting from the vibrations of molecules inside of pico cavities and reaching to the mirrors inside of gravitational wave interferometers [13]. The powerful thing about this Hamiltonian is that all optomechanical systems (with approximately linear coupling between optics and mechanics) can be described with it. The most simple setup for cavity optomechanical considerations is a basic Fabry-Perot cavity where one mirror is slightly movable by the radiation pressure of the light inside the cavity, this is a so called “mirror on a spring” system.

2.2.2 Membrane in the Middle Optomechanical Systems

Membrane in the middle (short: MIM) optomechanical systems are optical cavities with fixed mirrors and a movable membrane in between them. They can still be described with the same Hamiltonian, however the coupling constant G is calculated as shown in [8, p. 30 - 35]. Here the optical cavity frequency is calculated by finding the eigenmodes of the system for the particular boundary conditions on the different interfaces in the cavity. Alternatively the coupling can be understood by considering the shifting boundaries as a perturbation to the cavity field. This is depicted in Fig. 2.4. Here one can see that the coupling is maximized if an intensity maximum is present on one of the membrane surfaces whilst the other is in a minimum. This is because the effective index of refraction of the cavity mode is changing if the drum surface shifts. If the intensity is the same on both sides of the membrane the shifts cancel each other.

2.2.3 Fabrication of Polymer Resonators

To place such mechanical resonators inside of a fiber Fabry-Perot cavity, a commercially available micro 3D-Printing system by the company “Nanoscribe” is used (Fig. 2.3).¹ It prints “drums” with a size of about 50 – 100 μm , with surface features even significantly smaller than this at around 8 – 10 μm

¹ In cooperation with Alexander Faßbender from the research group of Professor Linden.

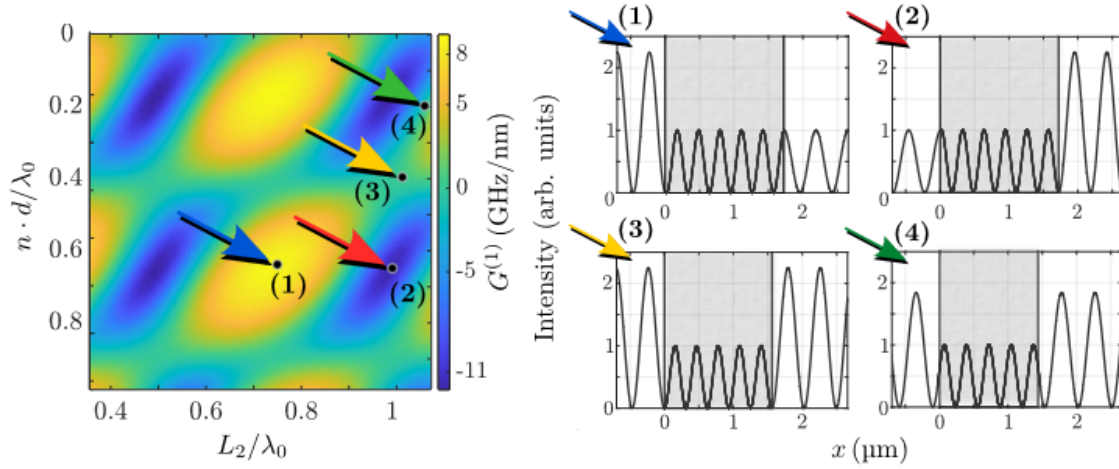


Figure 2.4: Taken from [8, p. 35]. Left: Map of the coupling, L_2 is the length of the mechanical oscillators feet, n is the index of refraction of the drum material and d is the drum thickness. Right: Four particular interesting spots of the map are selected, points of very high coupling in the forwards and backwards direction (1 and 2) and points of low coupling (3 and 4). The intensity distribution around the drum (grey) is shown.

either on a mirror substrate or on a fiber tip. To reach the capability of printing such tiny features that lay beyond the normal capabilities of the laser in the Nanoscribe system, a resin susceptible to photons double the frequency of the Nanoscribe laser is used and two-photon absorption, which only happens in regions of very high intensity in the beam, is utilized for a precision increase, the exposed parts of the resin then experience a photo polymerization process. This is explained in greater detail in [8, p. 15 -17]

2.3 Optomechanical Measurements and Cavity Locks

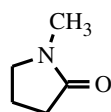
For experiments involving precise optomechanical measurements it is often important that the length of the cavity can be stabilized, so that external disruptions are compensated. Conceptually this can be achieved by a device that monitors the length shift of the cavity with an error signal and based on that sends a signal to a piezo that then corrects for this shift. Such devices are so called “PID-controllers”, the name originates from the fact that it considers the a proportional, an integral and a derivative term of the error signal for the calculation of the correction signal (technically the device we use is just a PI-controller, as it does not utilize the derivative of the signal). To work the PID-controller needs an error signal. An easy way to provide one is to just feed it the transmission (or in our case reflection) signal of the cavity. The PID-controller is then adjusted to stabilize the cavity on a flank of this, this process is called “side-of-fringe” locking. But being off resonant poses the problem that the power inside the cavity is lower than possible and that dispersive effects can optomechanically shift of the mechanical resonance frequency. This would not be the case if a lock in the center of the resonance were conducted. This can be achieved by the so called “Pound-Drever-Hall”-Lock that utilizes a phase modulator to optically create the derivative of the cavity signal. For simplicity all locks in this thesis were initially implemented with the side-of-fringe variant. The Pound-Drever-Hall locking scheme is explained in detail in [14, p. 193 - 197].

Building the Vacuum Fiber Microscope

3.1 Motivation for the Experiment

The central goal of our experiments is to explore the influence of mechanical resonators inside of single or double fiber Fabry-Perot cavities. The fiber mirrors that are part of the cavity, have their ends coated with a Bragg reflector (as explained in 2.1.2), an incoupling fiber with a transmission of 2000 ppm is utilized and the other fiber/mirror substrate used has a transmission of 10 ppm. The oscillators are printed either on a fiber tip or on a mirror substrate by a process explained in Sec. 2.2.3. In order to achieve a better mechanical quality in the resonator analysis, by excluding the dampening effect the air has on the drum oscillation, it is advantageous to place the cavities in vacuum, which led to a setup, used in the group previously, in which a so called “monolithic fiber cavity” is placed in vacuum. Our monolithic fiber cavities just consist of two fiber mirrors, with the already stated transmission. They are facing each other inside of a glass ferrule with a hole (131 μm) only slightly bigger than the fibers (125 μm). The glass ferrule is glued to a piezo and cut into three pieces to allow for scanning of the cavity, such a ferrule cavity is visible in Fig. 3.1. These monolithic cavities have the advantage of offering high passive stability because fiber movement is limited to a minimum in the small ferrule hole, and of being, because of their compact design, easily integrable into different experimental setups, like vacuum or cryogenic chambers. But they have the limitation that only one mechanical resonator can be positioned on the fiber tip and so a new ferrule cavity has to be built for every drum that is supposed to be examined. This takes a long time, as the fibers have to be selected at first, the drum has to be printed, the ferrule has to be glued to the piezo and has to be cut, the fibers have to be threaded through the ferrule and then the fibers have to be aligned and glued into place. Moreover, even though some efforts to dissolve the UV-glue that fixates the fibers in the ferrule with the strong organic solvent NMP¹ were made, fibers are still not reliably recoverable from the cavities and so after measuring just one drum two valuable fibers are lost. These time and resource consuming processes could be circumvented by removing the second fiber and building an experiment that works with a larger mirror instead, on which a substantial number of drums can be printed simultaneously. Even though a substantial amount of stability will be lost because the setup will not be monolithic anymore, the added flexibility through an easily accessible mirror with enough space for many more drums seems to be worth it. Additionally,

¹ Full name: N-Methyl-2-pyrrolidone, with the structural formula:



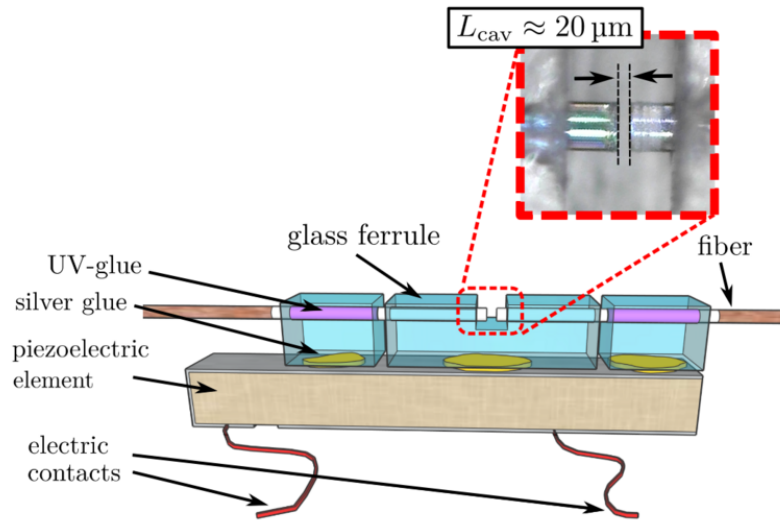


Figure 3.1: A sketch of the monolithic fiber Fabry-Perot cavities [8] (adapted from [15]). The ferrule is visible in blue and glued to the piezo below, the fibers are threaded into the ferrule and form a cavity at its center. The fibers are glued into place at the outside pieces of the ferrule but free to move in the inside section thus the cavity gets scannable when applying a piezo voltage.

it has been an interesting question how more complicated 3D-printed mechanical oscillator structures influence each other when interconnected and driven. So it seems only logical to build a vacuum setup that can deal with two fibers, a scanning and a driving one, capable of hovering over different parts of such a resonator structure on a mirror substrate, which led to the plan for the setup in this thesis.

3.2 Project Draft and Experimental Demands

As stated above, a system in vacuum is desired, capable of precisely positioning two optical fibers on top of a mirror substrate, with printed polymer resonators on it. Hannes Pfeiffer developed a detailed model in the engineering software “Inventor” of how that can be realized (Fig. 3.2). We will call this the “inner setup” from now on. It consists of five vacuum compatible linear translation tables (also called “translation stages”) made by “Physical Instruments”. Three are the shorter M-111 and two the longer M-112 variant with 15 mm and 25 mm movement range respectively [16]. These stages have a minimal step size of 50 nm and will be responsible for precisely positioning the fibers over the mirror substrate.

The mirror substrate is supposed to be attached to the “Motorized vacuum compatible Rotation Stage” made by “Newport”, visible in yellow on the bottom of Fig. 3.2. The structural components of the inner setup will be made of aluminum which the different active components are screwed to, these structural components are then connected to mounting holes in a modified CF DN 160 reducing flange on top which is itself connected to a 6-Way DN 63 cross that handles all the necessary feedthroughs.

From now on the stages will follow a numbering convention, which is visible in Fig. 3.3. The stages 3 and 5 are the M-112 variant. The stages 1,2,4 are shorter M-111 ones. Stage 0 is the rotation stage.

The idea is to have the inner structure connected to a flange on top that handles all electrical and optical feedthroughs, and to position this in an outer protective structure for assembly and maintenance

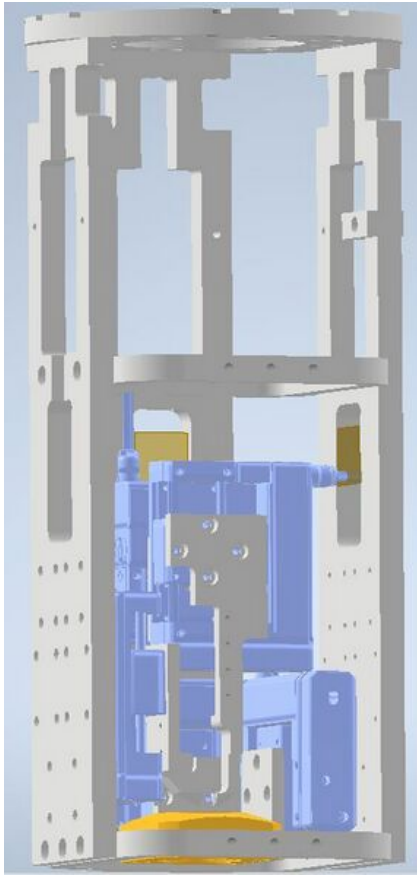


Figure 3.2: Inventor model of the inner structure.

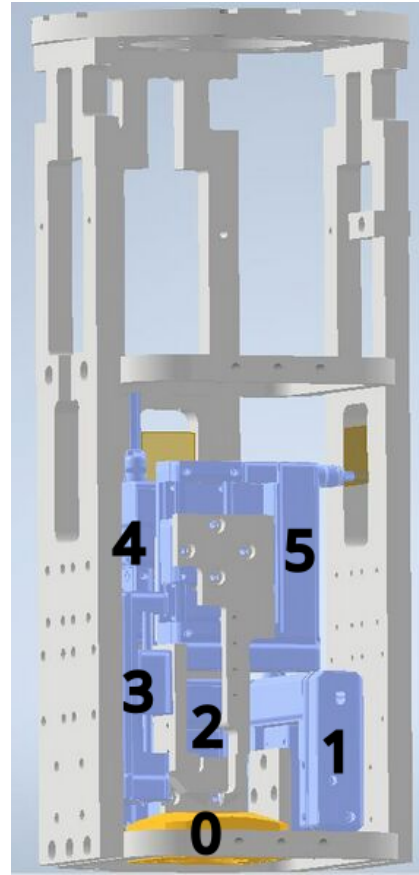


Figure 3.3: The stage numbering convention.

(called the “outer structure” from now on). The inner setup with its flange on top will then be lifted out of the support and moved into the vacuum chamber for usage. The mirror substrate holding rotation stage is connected to stage 1 which is itself connected to stage 2 and thus the mirror substrate can be freely positioned horizontally and rotated around. Stage 3 carries the first fiber holder and is responsible for lowering it to the right position to form a cavity with the mirror substrate, it is thus controlling the cavity length of the first fiber mirror. Stage 5 is screwed to stage 4 and controls the height of the second fiber mirror above the substrate, while stage 4 controls the distance between the fibers. Note that the two fibers only have this one relative degree of freedom but can, because of the rotation stage, still be positioned arbitrarily on the substrate.

3.3 Construction

3.3.1 Structural Construction

The first step in the construction of the fiber microscope was the assembling of the outer protective structure that is able to hold the inner part of the microscope and keep it clean and separated from the environment to achieve a good vacuum later on. The support structure consists of an aluminum

breadboard, on which four Rose-Kruger aluminum frames were screwed to orthogonally, plexiglass panels between the frames and four further frames that connect everything at the top. Next, there is an aluminum plate with a hole that allows for the top vacuum flange, which hosts all the feedthroughs, to rest on the plate and the inner setup to hang downwards through the hole into the protective outer structure. On the aluminum plate a clean rubber gasket was added around the hole for safe contact to the vacuum flange without damaging its cutting edge and easy vertical removal of the inner setup for introduction into vacuum by just pulling the flange upwards (Fig. 3.4).

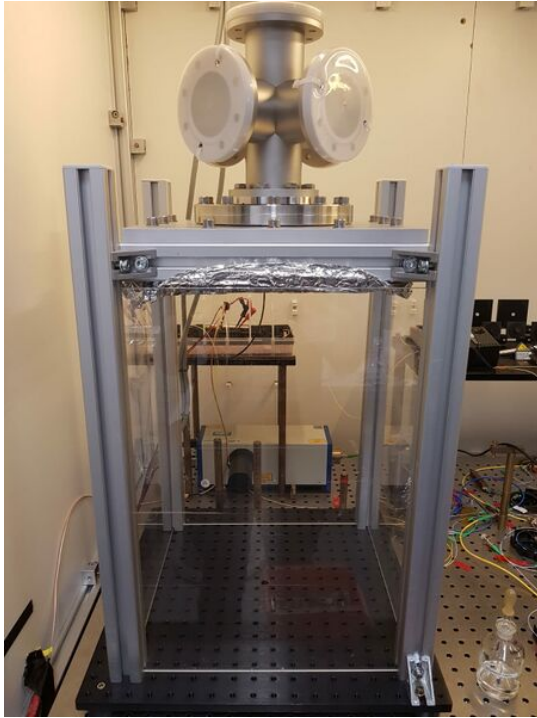


Figure 3.4: The basic outer support and protection structure. One can see the aluminum scaffolding on the sides, the 6-Way cross at the top and the aluminum breadboard at the bottom.



Figure 3.5: The basic outer support and protection structure with the inner frame for stage attachment partially assembled.

After the outer structure was assembled, the aluminum parts of the inner structure were screwed to the top flange and connected with each other via aluminum loops (Fig. 3.5).

3.3.2 Mechanical and Electrical Construction

After the inner support structure for the active components was assembled, the stage interfacing was tested with the included software for the translation stages PIMikroMove®. To do that the stages (Fig. 3.6) were connected to a controller (Fig. 3.7). Conveniently all 5 controllers (one for every translation stage) can be connected in a daisy chain and thus only one controller has to be connected to the pc, the stage daisy chain can then be added to the software via clicking the dialog visible in Fig. 3.8.

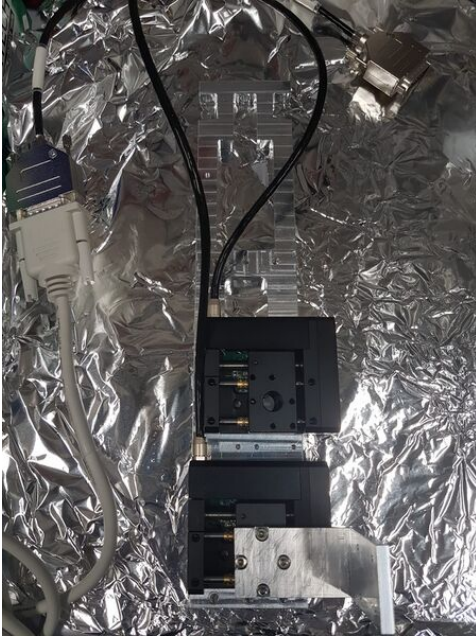


Figure 3.6: The stages 2 and 4 hooked to their controller for first interface testing.



Figure 3.7: One of the translation stage controllers.

After the translation stages were tested, the controllers were positioned on top of each other to form a controller stack (Fig. 3.10). Then it was begun to assemble the stages into the setup (Fig. 3.11). At first only the lower three translation stages were placed (Fig. 3.12), as it is sufficient for a basic functionality of the setup (controlling just one fiber over the substrate), and the rotation stage was added (Fig. 3.13). But shortly after it was decided to place also stage 4 and 5 (the remaining two translation stages) already, as it would be way more difficult to assemble them in a subsequent state of the experiment (Fig. 3.18).

After that, the cables controlling the first three translation stages were connected to special feedthrough flanges (Fig. 3.9) and those were screwed to the cross flange. To connect the rotation stage (Fig. 3.14) to a vacuum feedthrough proved a bit more difficult, as the cable was vacuum safe but the cable connector was not, and so the cable had to be cut (Fig. 3.15). As it was a coaxial one, the outer conductor was twisted to free the inner conductor and then both of them were connected to a basic DN 40 copper rod electrical feedthrough. These were attached to the 6-Way cross by placing a reducing flange between the DN 40 copper rod feedthrough and the DN 63 cross. The outside part of the rotation stage cable was temporarily attached with crocodile clamps (Fig. 3.16), while the inner part was attached with CuBe-Connectors. Later, a more permanent solution, involving a jumper cable, soldered to the inner conductor, and screw terminals, was built for the outside connection (Fig 3.17).

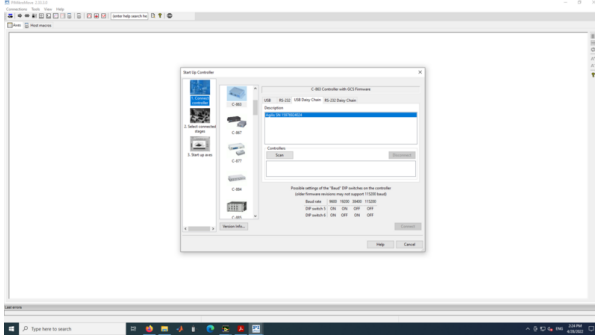


Figure 3.8: The MicroMove[®] interface to add the stage daisy chain.



Figure 3.9: The custom translation stage feedthroughs.

Chronologically the next step was to build the fiber holders, which is described in Sec. 3.5. After they were completed and a fiber mirror was threaded into the first holder's ferrule, the feedthrough for stage 4 and 5 (Fig. 3.19 and Fig. 3.22) was also added alongside the feedthrough for the cables interfacing the piezo of the fiber holder, they were coupled using CuBe-connectors (Fig. 3.21). The feedthrough was not connected to the cables of the fiber holder directly, but was instead fitted with only Kapton[®] coated copper cables that reach down to the stages so that the fiber holder can be more easily attached and removed without having to detach the feedthrough flange at the top every time.

Then the first finished fiber holder was screwed to stage 3 and the piezo cables were connected. The fiber in the holder was pushed through a Swagelok gas inlet that, together with a custom conical Teflon piece with two holes, was repurposed as a fiber feedthrough (Fig. 3.20). The second hole is intended for the second fiber mirror and was temporarily blocked with an old broken fiber piece. After the fiber holder was attached and the fiber itself pushed through the Swagelok connector, the fiber had to be spliced to an optical patch cable for interfacing the laser, this was done using the "Fujikura ArcMaster FSM-100P+" splicing machine (Fig. 3.23). For that the fiber was first spliced to an elongation, the elongation and the fiber mirror itself are copper coated to increase their mechanical stability, so around the fiber ends this coating was stripped with an Fe(III)Cl solution (Fig. 3.24). After that, the two fibers were just placed in the splicer and a fitting splice program for their 125 μm thickness was started (Fig. 3.25). Then the elongation was spliced to an optical patch cable almost the same way, with the exception that the patch cable has a plastic coating that is not chemically removed, but instead just mechanically using dedicated tools (Fig. 3.26).



Figure 3.10: The whole translation stage controller stack in the daisy chain configuration. The individual controllers were connected to each other and one had to input their binary address in the daisy chain by switching their “Addr.”-buttons.



Figure 3.11: The inner aluminum structure with the first translation stage that will control the left fiber.

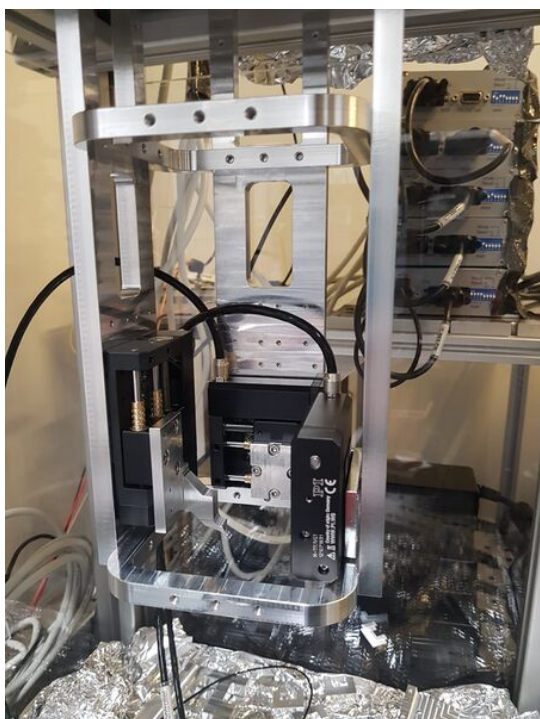


Figure 3.12: The first three translation stages, which are the ones needed for the simplified one fiber setup, were assembled and attached to the main aluminum frame. The control units are visible in the background.



Figure 3.13: Complete assembly of the basic setups inner structure, now with the rotation stage attached.



Figure 3.14: The rotation stage that will hold the mirror substrate for the experiment.



Figure 3.15: Cut rotation stage cable stripped of isolation and with twisted outer conductor.

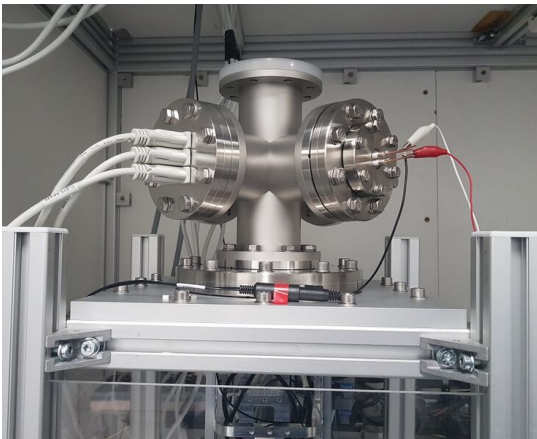


Figure 3.16: The 6-Way cross in its first testing configuration. The left flange allows interface to the translation stages 1-3 and the right one carries the electrical feedthrough for the rotation stage. Flanges for fiber feedthrough, piezo control and interface of stage 4 and 5 are still missing.

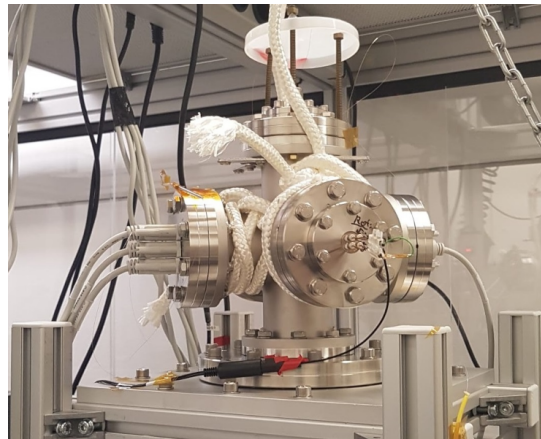


Figure 3.17: The top 6-Way cross in its final configuration, the connection to the electrical feedthrough of the rotation stage was made more permanent and a cap was added for protecting the fiber during transport (Sec. 3.6.2).



Figure 3.18: As stage 5 had to be mounted to stage 4, an aluminum connection block was necessary, the through holes of stage 5 were used with brass screws to interface it.

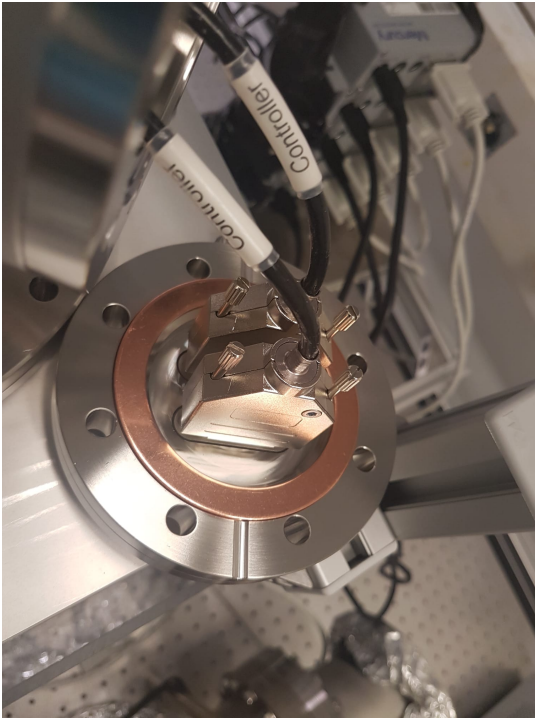


Figure 3.19: The feedthrough flange for stage 4 and stage 5.



Figure 3.20: A Swagelok gas inlet repurposed as a fiber feedthrough.

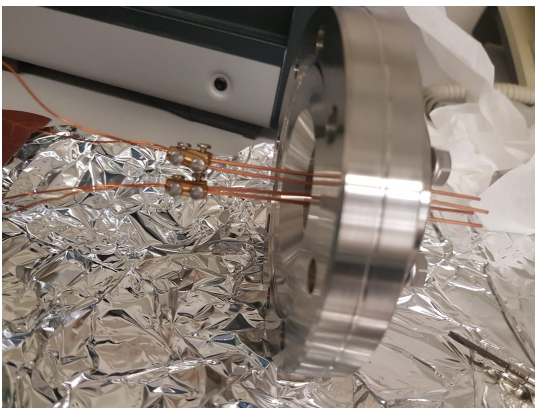


Figure 3.21: The copper rod feedthrough for the piezos, connected to Kapton[®] coated copper cables using CuBe-connectors.

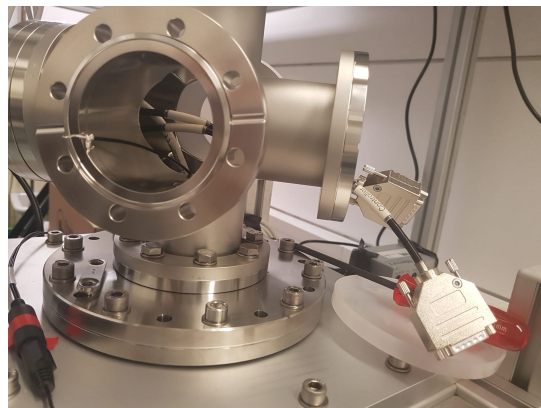


Figure 3.22: The 6-Way cross with the cables for stages 4 and 5 hanging out.



Figure 3.23: The “Fujikura ArcMaster FSM-100P+” splicer.

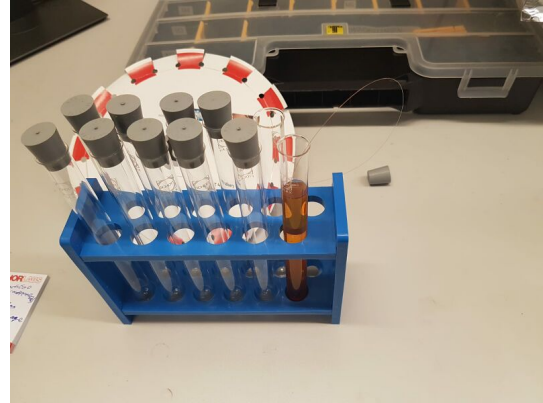


Figure 3.24: A fiber placed in an Fe(III)Cl solution.

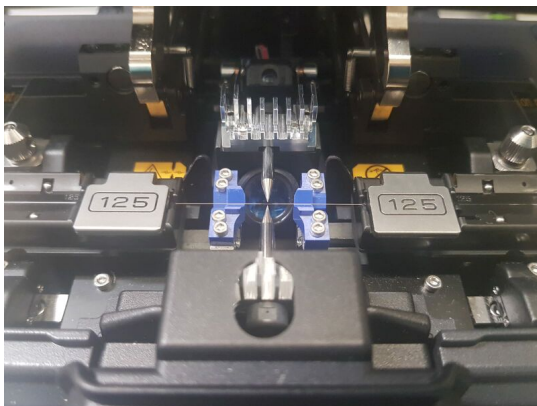


Figure 3.25: Fiber mirror and elongation are spliced together in the Fujikura splicer. The two fibers intended for splicing were clamped into the dedicated holders, visible on the sides, and the two central electrodes will provide an arc that fuses the fibers together.



Figure 3.26: The tools necessary to strip an optical patch cable of its isolation, special pliers for the outside isolation (right) and a dedicated stripper for the inside one (left).

3.4 Coding a Control Software

An essential part of the experiment was to create a central application, capable of running all the setup's individual devices. For this the “Vacuum fiber microscope control unit” was programmed. It utilizes the python gui package “Tkinter” to create a graphical interface for stage control and microscope view. The interface to the translation stages is achieved by the python package “picontrol”, made by “Physical Instruments” for controlling their products. The whole controller stack can be connected at once by using a command for USB-daisy chain connection. To interface the rotation stage proved to be a bit more complicated as no such package was existent and a serial connection had to be established via the python “serial” package, but as the commands were documented and less complicated than the ones of the translation stages, it worked without any issues. Then methods for moving the stages relative and absolutely, as well as stopping them and deactivating the servos in the translation stages for better position stability (useful when measuring with the setup), were added and made callable by button press in the control interface. Lastly, an effort was conducted to make the window nicely resizable and to incorporate the camera image without lag into the control software window, which worked relatively well thanks to the “PIL” and “cv2” package, but a little lag remains sometimes, especially on position reading. In the future further optimizing and effectively multi threading the program will be an objective. The interface window in its current form is visible in Fig. 3.27.

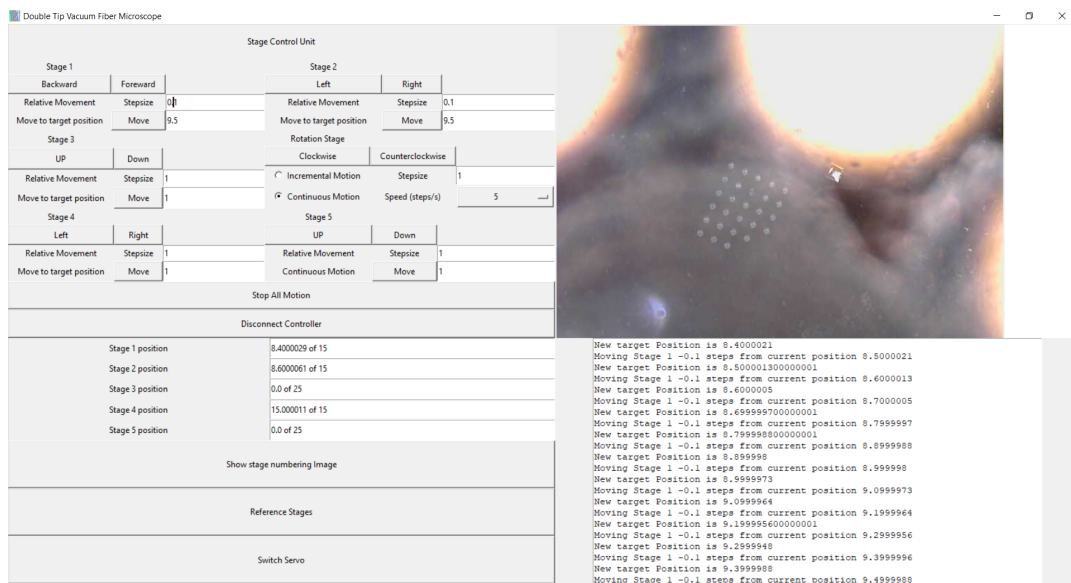


Figure 3.27: The fully functional control interface window with a live view of the mirror substrate, and a console printing a message about every action conducted, on the right, and control buttons for repositioning, servo switching, and controller disconnection, as well as displays for position monitoring, on the left.

3.5 Building Fiber Holders

The holders, used for placing the fiber mirrors above the mirror substrate, consist of an aluminum base, which a glass ferrule is then glued on. The ferrule has a borehole of $131\ \mu\text{m}$, only slightly bigger than the

fiber at 125 μm . This helps to effectively stabilize the fiber, similar to the monolithic fiber cavities (Fig. 3.31). In fact, the ferrule used here for keeping the fiber into place on the holder is a fragment of one that would have been used for monolithic fiber cavity manufacturing. On a platform a few millimeters in front of the ferrule Macor[®] ceramic plates, cut from a larger piece visible in Fig. 3.38, were attached on which a piezoelectric element was placed to allow for cavity length scanning (Fig. 3.30). The ceramic is necessary to not shorten the piezo with the aluminum holder. After that the piezo was electrically interfaced with two Kapton[®] coated copper wires. These components were attached with a strong conductive silver glue (Fig. 3.28), it was applied using needles and then baked in an oven to harden. This procedure was conducted for both the fiber holders that were needed for the full experiment (Fig. 3.40 and Fig. 3.41).



Figure 3.28: The two-component silver glue used.



Figure 3.29: The UV-glue used.

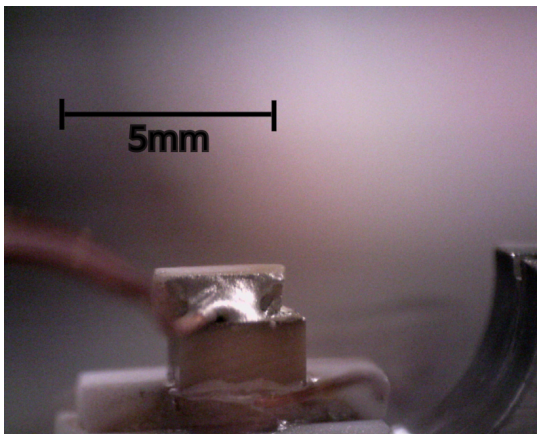


Figure 3.30: A microscope image of the isolation, the piezo and the piezo wires on the holder.

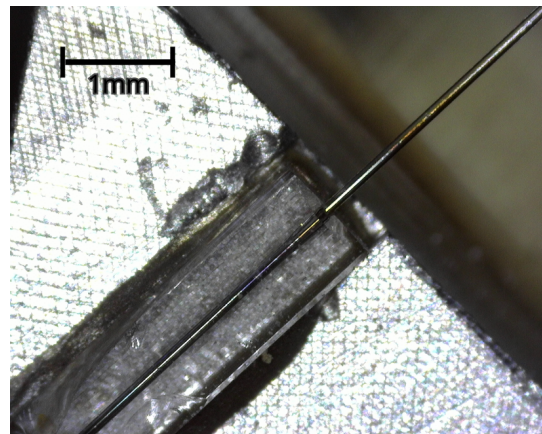


Figure 3.31: The ferrule glued in the fiber holder base with the fiber mirror threaded in. One sees the back end of the ferrule, further on the top right the piezo is located and further down left the fiber mirror tip peaks out the ferrule for a few millimeters.

After the fiber holders were assembled, good fiber mirrors had to be found for them. This was achieved by first selecting fresh fibers from the stockpile holder (Fig. 3.34) and testing them in a basic



Figure 3.32: The basic mirror testing setup, consisting just of a fiber mirror, attached to a manual translation stage, and a mirror substrate.

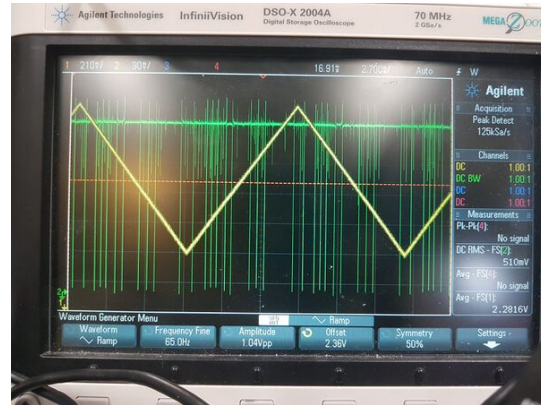


Figure 3.33: Deep cavity dips imply a strong coupling and give first indications that the fiber is working correctly.

configuration consisting of just a manual ThorLabs translation stage with an integrated piezo and a mirror mounted in front of it (Fig. 3.32). The back reflection dips of the cavity built this way were observed (Fig. 3.33) and the finesse was estimated, two promising fibers were thereafter fully measured (Sec. 4.1.1). They were both deemed sufficient and the first one, called “fiber1” from now on, was threaded through the ferrule of the first holder, as just a single fiber holder is needed for the basic functionality of the setup, the second one, now called “fiber2”, was temporarily stored on the side.

The fiber mirror now had to be threaded through the ferrule, this was done by placing two Thor-Labs 3D translation stages in direct proximity and mounting the fiber and the holder on one of them respectively. The ferrule was then viewed through two USB-microscopes and the fiber was carefully moved to the ferrule. After reaching the ferrule, the fiber had to be aligned with the borehole in the ferrule (Fig. 3.37) and following this it was cautiously moved inwards, the ferrule hole has little conical ends which are very helpful for this task. After the fiber was introduced, UV-glue (Fig. 3.29) was prepared and applied to the piezo with a thin Thorlabs tungsten cleaning wire to connect the fiber to it. After the glue was applied a UV-lamp was placed above the threading setup to harden it (Fig. 3.36).

As some of the first gluing attempts didn’t work out ideally, because excess silver glue was blocking the fiber path in the ferrule or the piezo was shorted out because of it, excess glue had to be removed a few times with a dental drill (Fig. 3.35 and Fig. 3.39).

After the fiber was glued into place (Fig. 3.42 and Fig. 3.43), the holder was built into the setup and the fiber was spliced to an optical patch cable and tested, during testing a collision of the fiber in the holder (fiber1) with a USB-camera happened and the fiber broke, so the UV-glue was removed again, also with the dental drill, and instead of fiber1, fiber2 was threaded into the first fiber holder and glued into place. This was the configuration used for the rest of the experiment.



Figure 3.34: The fiber stockpile holder in which the fibers are placed when they arrive from the coating company.



Figure 3.35: The dental drill.

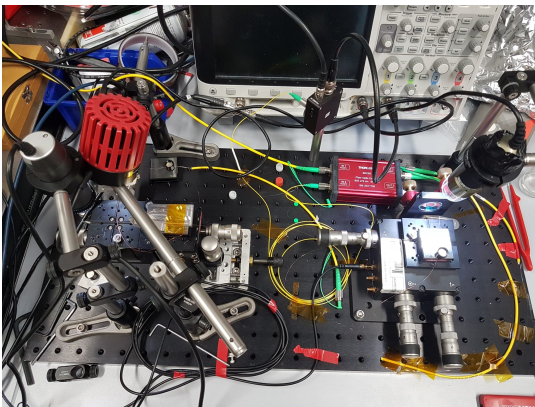
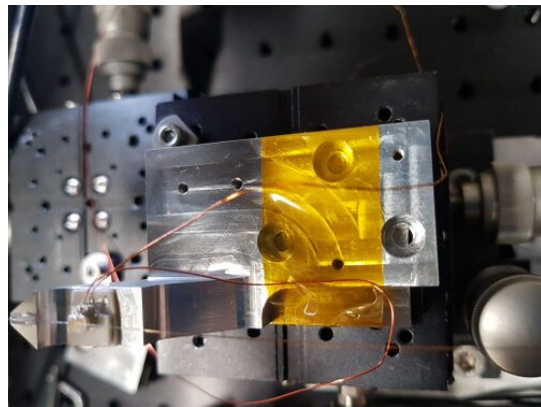


Figure 3.36: The fiber threading (left) and basic mirror testing setup (right), a UV-lamp is placed above the fiber holder for curing of the UV-glu



after threading.

Figure 3.37: The fiber holder while the ferrule is threaded through.



Figure 3.38: The Macor[®] Ceramic plates used in building the fiber holders for piezo isolation.

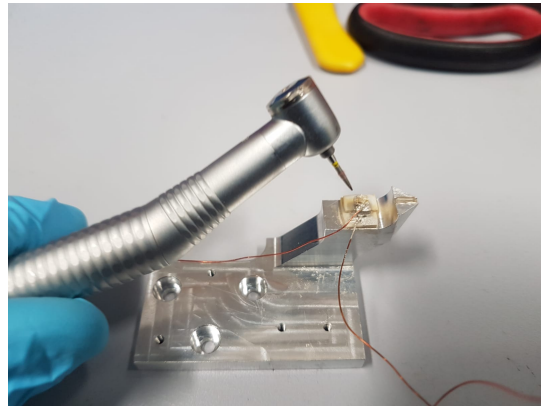


Figure 3.39: The dental drill is being used for removing excess material.

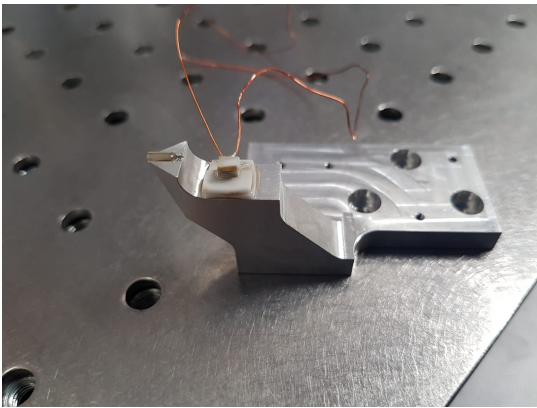


Figure 3.40: The finished first fiber holder, with the ferrule at its tip and the piezo positioned further to the right. The fiber is not introduced yet.



Figure 3.41: The second fiber holder that will place the second fiber above the mirror substrate as soon as the experimental setup is completed. Piezo and ferrule are visible on the right.



Figure 3.42: The UV-glue as it was applied to the piezo to fixate fiber1.

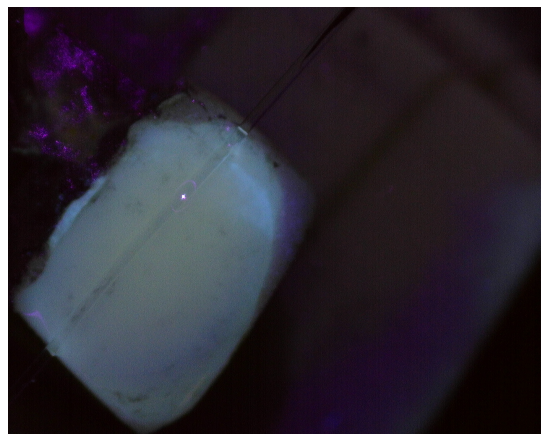


Figure 3.43: The UV-glue while curing under the UV-lamp.

3.6 Integration into Vacuum System

3.6.1 Building the Vacuum System

The vacuum system consists of a main experiment chamber (a CF DN 160 T-piece), in which the inner structure, assembled in the outside holder, will be placed, and a second larger chamber for interfacing the two pumps used (a CF DN 100 T-piece), a turbomolecular pump and an ion pump. Various further flanges (of CF DN 40 size) form a connection between these primary components. There is also a small secondary experiment chamber for later continuing efforts to study monolithic fiber on fiber cavities, as their study was the primary objective of a previous vacuum system, from where most of the components are reused now, and that functionality should not be lost. The main experiment chamber also has a view port at the bottom, so the mirror substrate can be observed when the experiment is in vacuum. The chambers are separated into three sections by two valves, the first valve separates the turbomolecular pump from the rest of the setup for easy pump down performance testing and the second valve separates the main experiment chamber, so that not the whole vacuum chamber has to be pressurized if maintenance on the experiment is required. A sketch of the setup is visible in Fig. 3.44. It was begun by

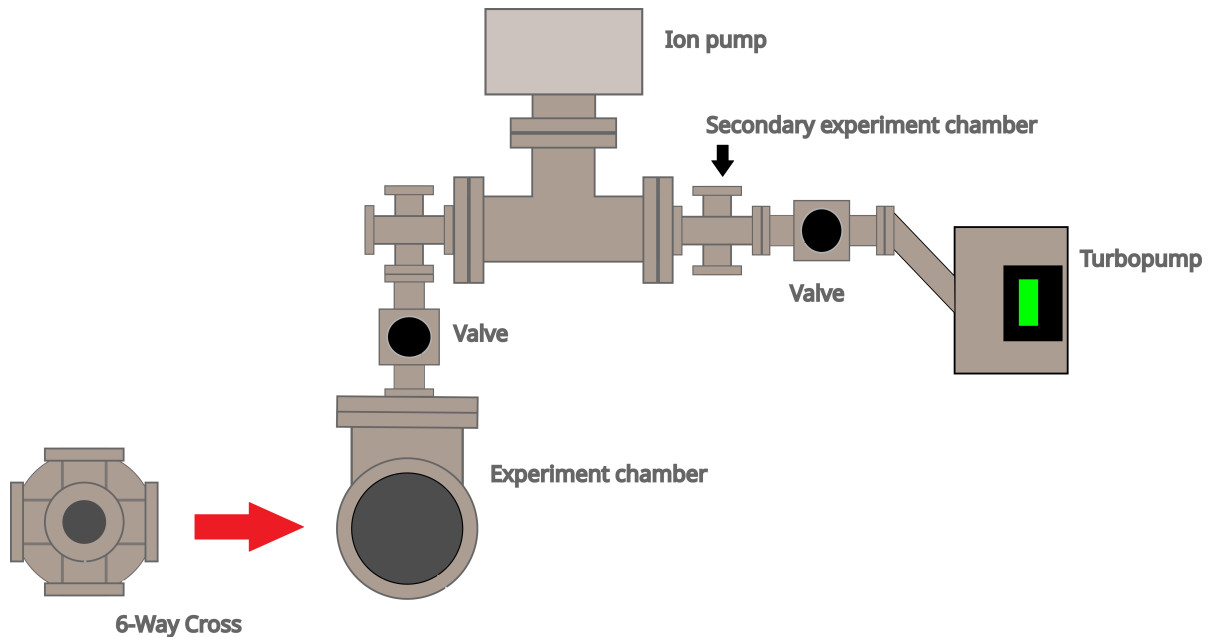


Figure 3.44: A sketch of the vacuum system structure.

first assembling the right part visible on the sketch: a DN 100 T-piece, the ion pump, the turbopump, a DN 40 4 cross flange (the secondary experiment chamber (Fig. 3.45)) and a valve between the cross and the pump's metal tube (Fig. 3.46). A first pump down showed that there was no leakage, then another 4 cross and a 90° angled tube were attached, after that another valve and the main experiment chamber were added (Fig. 3.47 and Fig. 3.51 and Fig. 3.49). After that the experiment chamber was closed off with a blind flange (Fig. 3.50) and another pump down test was started, as we were able to reach $5.07 \cdot 10^{-7}$ mbar relatively quickly (Fig. 3.48) the chamber seemed to be free of leakage and relatively clean. After that, the blind flange was removed again and the experiment was prepared for vacuum.

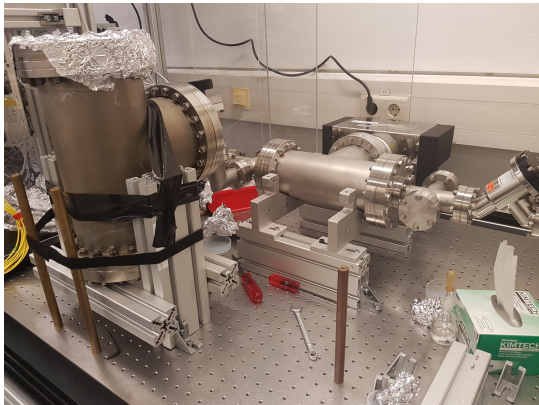


Figure 3.49: View onto the whole vacuum setup, with the experiment chamber attached.

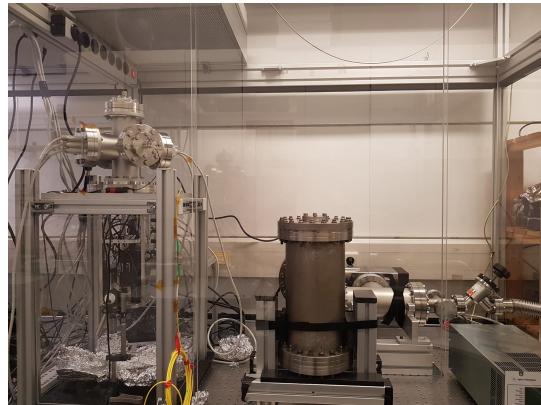


Figure 3.50: The whole experimental setup up to this point, the vacuum chamber now has a blind flange on top.

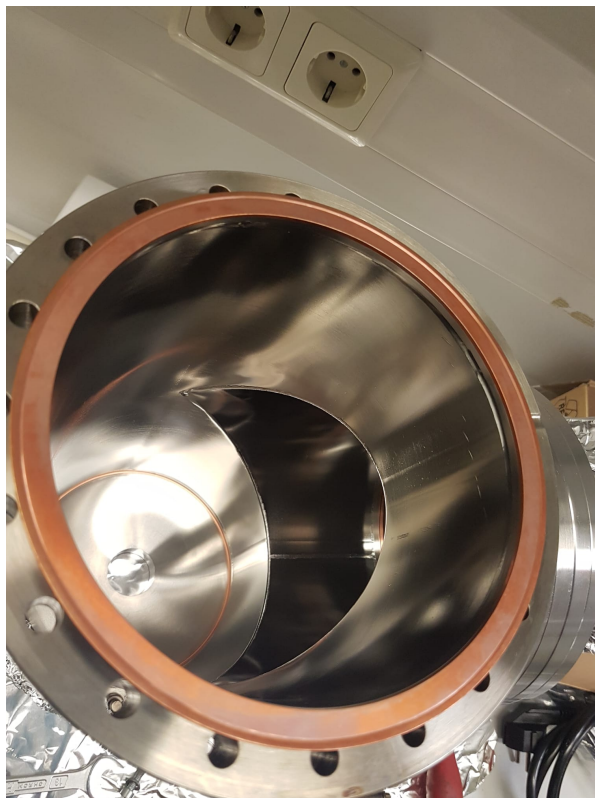


Figure 3.51: Sight into the main experiment chamber, before the view port is screwed on.

3.6.2 Constructing a Transport for Introduction to Vacuum

The inner structure, carrying the experiment, has to be lifted out of the outer support and transported to the experiment chamber next to it, all without damaging the fiber at its feedthrough, as this section is quite delicate. This was achieved by installing a rail, hosting a hoist above the experiment. This hoist can be moved over the experiment area and is connected to the inner setup's flange via nautical knots in a nylon rope (Fig. 3.52 and Fig. 3.59). A little plastic cap on three threaded rods was attached to the top flange to protect the fiber from the rope (Fig. 3.17).



Figure 3.52: The rail and hoist used for inner structure transportation.

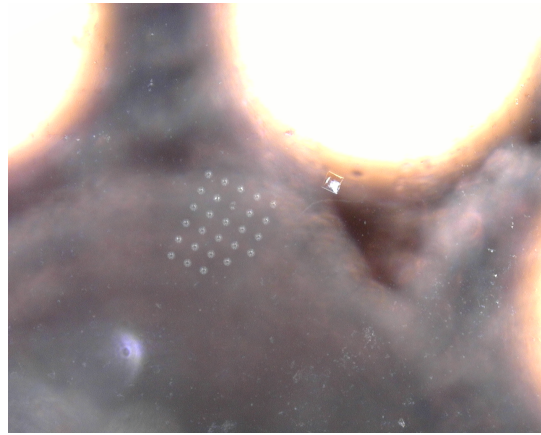


Figure 3.53: Some polymer drums as seen through the view port with an USB-microscope.

3.6.3 Moving the Experiment into the Vacuum Chamber

To move the experiment into the vacuum chamber the outer structure was partially disassembled, so that the aluminum plate, the top flange is resting on, can be lowered deep enough in order for the inner setup, hanging from the rope, to be lifted out (Fig. 3.54). Then the setup was pulled up and moved along the rail towards the experiment chamber (Fig. 3.55) and after that lowered into it (Fig. 3.56). Then the chamber was closed and screwed tightly and a pump down test was started. After about two weeks of pumping with the turbopump a pressure of $2.6 \cdot 10^{-6}$ mbar was reached (Fig. 3.57). This is already mostly sufficient for the desired optomechanical purposes but could imply that the inner setup was a bit dirty or one of the flanges does not sit perfectly tight, the pressure will further improve once the ion pump is activated, too. The rotation stage and, with an USB-microscope, also the drums on the mirror substrate were visible through the view port (Fig. 3.58 and Fig. 3.53).

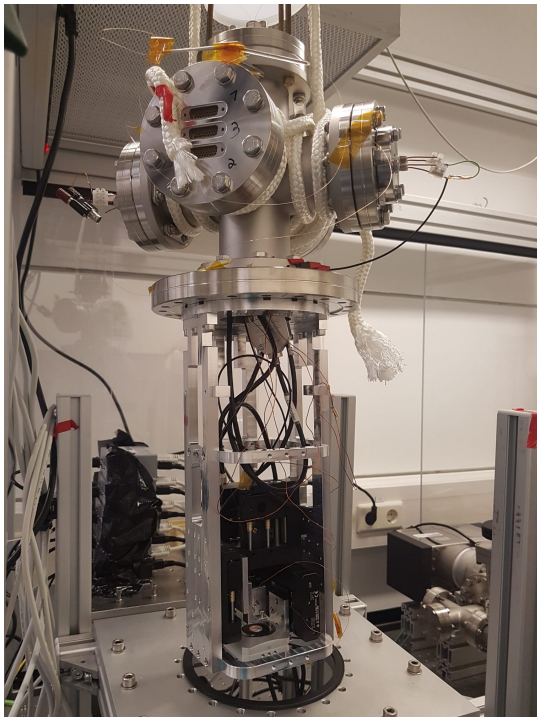


Figure 3.54: The inner setup hovering over the lowered aluminum plate of the outer protective structure.

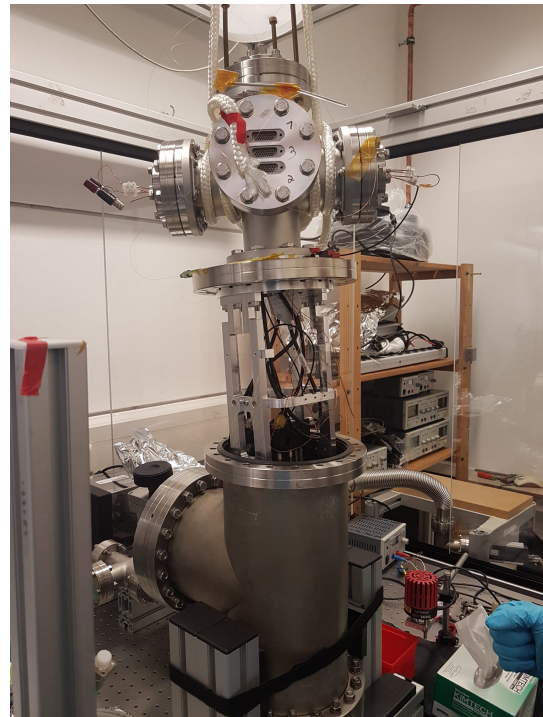


Figure 3.55: The experimental setup was moved to the vacuum chamber.



Figure 3.56: The inner setup was lowered into the vacuum chamber.



Figure 3.57: A pressure reading after two weeks of pumping with the turbopump of $2.6 \cdot 10^{-6}$ mbar.

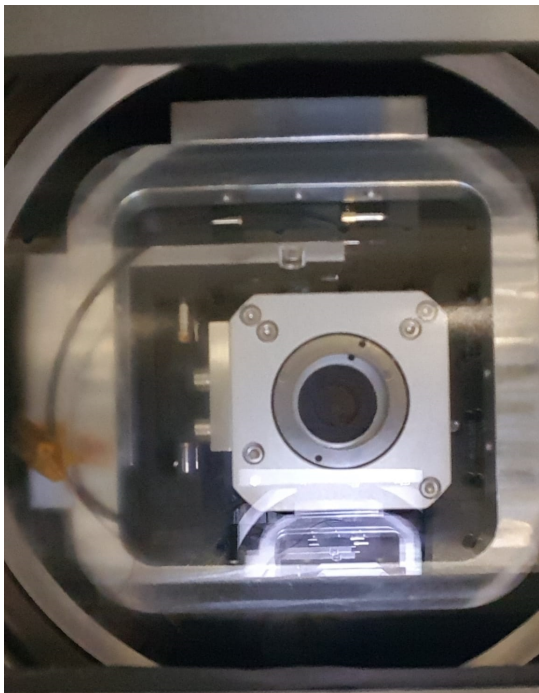


Figure 3.58: The mirror substrate as seen from the viewport on the bottom of the experiment chamber.

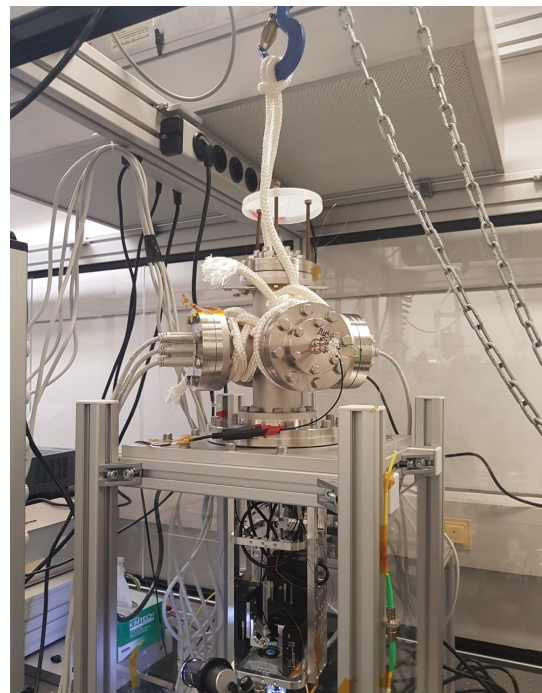


Figure 3.59: The inner structure connected to the hoist.

3.7 Efforts to Stabilize the Cavity

As first measurements with the system were pretty unstable and a reliable lock was not achievable, an additional structure was needed to stabilize the cavity for locking. The problem probably lies in the fact that stage 3 and the rotation stage are not strongly mechanically connected and thus slightly oscillate relative to each other, this is made worse through the circumstance that the rotation stage is only connected to stage 1 on the right side and this is then connected to stage 2, which means there are substantial lever forces playing a role. A stronger mechanical connection between rotation stage and stage 3 can improve the stability significantly. With the help of Hannes Pfeiffer an L-piece was designed to connect the fiber holder on stage 3 with a screw to the rotation stage, carrying the mirror substrate (Fig. 3.60 and 3.61) and thus limiting the amount of possible relative oscillation. Luckily there already were some threaded M2 holes in the fiber holder, initially intended for fixating cables, which were ideal for attaching the L-piece. Initially it was tried to place UV-glue on the end of the screw to have a softer

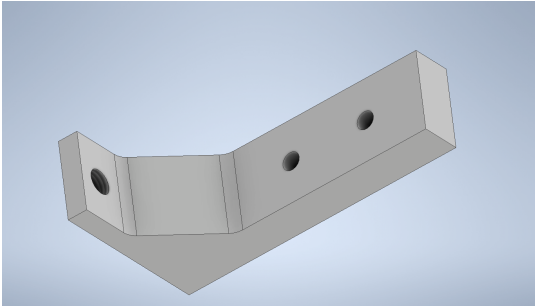


Figure 3.60: The L-piece in “Inventor”.

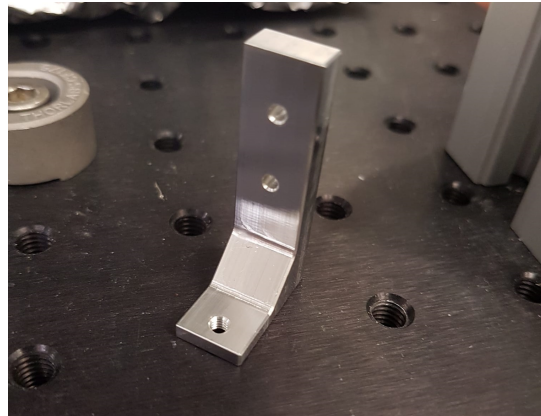


Figure 3.61: The L-piece with a threaded M3 hole for holding the stabilization screw and two M2 through holes for connection to the fiber holder on stage 3.

contact point, but as the screw, for normal modes of operation, does not touch the mirror substrate but only the rotation stage and the glue was not adhering very well to the screw, it was left out (Fig. 3.62 and Fig. 3.63). With the screw correctly positioned, the cavity became much more stable and lockable.

3.8 Future Extensions

Possibilities for future setup improvement begin with building better observation optics for the experiment in vacuum. A 45° tilted mirror, installed at the right height on the aluminum frame of the inner structure, could prove useful for observing the fiber. Currently only an image from directly below the fiber and mirror substrate can be taken. This is enough for fiber positioning above it, as the substrate is sufficiently transparent for visible light, but does not provide any information on the fiber height, which imposes the danger of incautiously lowering the fiber too deep and in consequence crashing it.

A second possibility for improvement considers the hoist mechanism as it does not reach high enough and so the setup has to be lifted a few centimeters by hand into the vacuum chamber, this will be fixed by



Figure 3.62: The L-piece with screw and UV-glove at its tip.

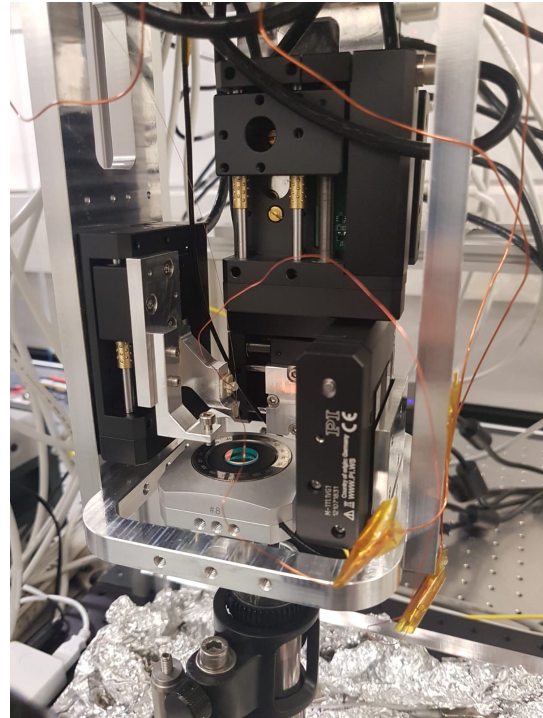


Figure 3.63: The L-piece attached to its desired position on the first fiber holder.

either modifying the rope configuration at the top or by ordering a custom aluminum part that clamps over the flange sides and provides a hole for the hook of the hoist to go through.

Thirdly, the current cavity stabilization method using a screw isn't ideal, as it requires manual intervention when the cavity length is supposed to be changed, which is obviously impractical when the setup is in vacuum. Thus, an electrically controlled vacuum compatible linear extending piston will be used to precisely control the cavity stabilization in the future.

The main extension plan though lies in completing the initial experiment idea by gluing a fiber mirror to the second holder and installing it into the setup to get the possibility of dual cavity operation and allowing experiments for investigating arrays of coupled polymer resonators to begin.

Lastly, further software optimization (as stated in 3.4) can be useful, eliminating the lag in the camera image that occurs sometimes, and possibly also adding further features, for example camera image post processing to allow for a better visibility of the polymer resonators. If the plan for attaching a 45° tilted mirror works out, a second camera is needed to observe the fiber and therefore the software should be extended to incorporate this as well.

First Measurements and Optimizations

4.1 Finesse Measurement Procedure

The general setup for the finesse measurements, conducted in this thesis, consists of a beam splitter (Fig. 4.1) and a photo diode (Fig. 4.2). The laser is connected to the beam splitter. The experimental setup is connected to one of the output sides, on the input side the photo diode is connected to the second entry so that it can monitor the reflection signal from the fiber mirror. When the experiment cavity, built by the fiber mirror and mirror substrate reaches a resonant length through the piezo scan (a triangular waveform voltage of about $400 V_{pp}$ is applied to the piezo) a cavity resonance dip appears in the back reflection signal from the photo diode. Two different methods for conducting the finesse measurements were used. They both require a region with linear piezo scan (this is usually realized if the extrema of the triangular waveform are avoided). The first one utilizes the temporal distance between two reflection dips of subsequent longitudinal cavity modes that are separated by a free spectral range, thus the time axis of the oscilloscope can be calibrated and identified with a frequency axis by measuring the cavity length and utilizing that the free spectral range is just $\frac{c}{2L}$.

The second measurement technique uses an electro-optical modulator (Fig. 4.3) to impose sidebands on the laser resulting in additional cavity dips. EOMs work by a crystal that can change its refractive index, based on an electric field acting on it, this field is created by a waveform applied to a capacitor (further details can be found in [6, p. 418-424]). This waveform was created by the function generator shown in Fig. 4.4. The temporal distance of these sidedips in the oscillogram depends on the frequency of the electrical signal applied to the EOM. Thus, the time axis of the oscilloscope can be calibrated and identified with a frequency axis again and the FWHM can be determined.

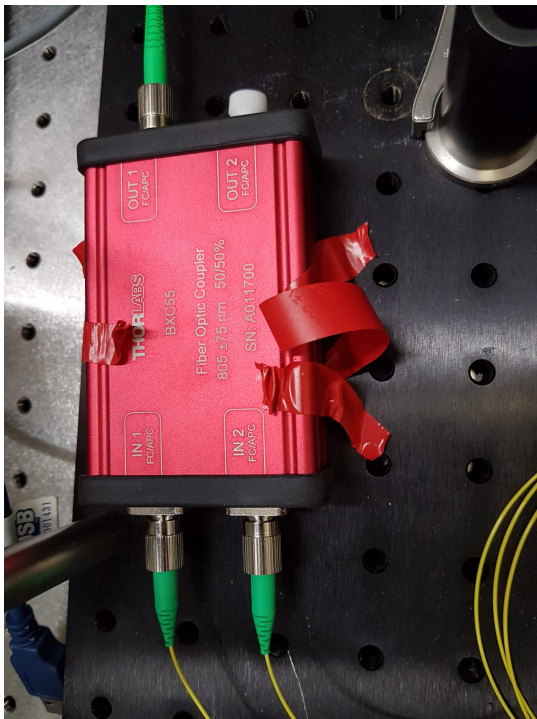


Figure 4.1: The beam splitter used in the experiment.



Figure 4.2: An image of the photo diode used in the experiment.



Figure 4.3: An image of the electro-optical modulator.



Figure 4.4: The function generator that drives the EOM.

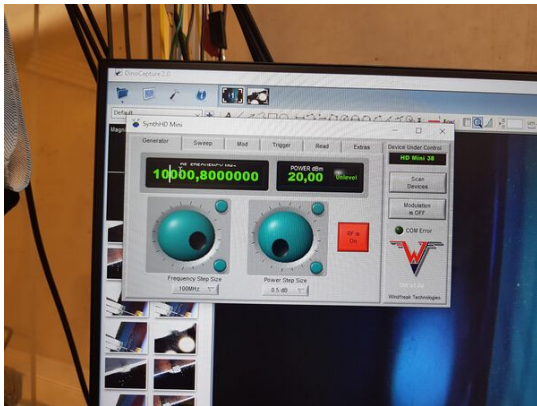


Figure 4.5: The control interface for the waveform generator that feeds the EOM.

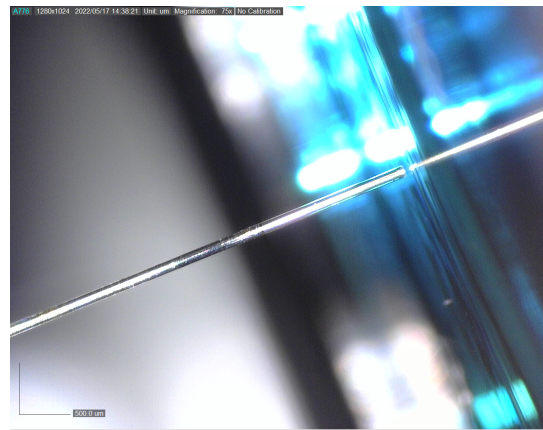


Figure 4.6: A microscope image of a fiber in the basic mirror testing setup.

4.1.1 Measurements of Fiber Candidates

To determine which fiber mirrors from the stock had a quality high enough for use in the experiment, the fibers were introduced in a basic testing setup. This was done by splicing them to an optical patch cable, connecting that and a photo diode to the beam splitter, as described above, and then placing them with a manual translation stage, fitted with a piezo, in front of a mirror substrate to form a cavity (Fig. 4.6). The finesse was then measured ten times with the FSR-method and, to minimize fluctuations, the variance weighted mean was calculated according to:

$$\bar{x} = \frac{\sum_{i=1}^N \frac{x_i}{\Delta x_i^2}}{\sum_{i=1}^N \frac{1}{\Delta x_i^2}} \quad (4.1)$$

Gaussian error propagation shows that the uncertainty of the weighted mean is:

$$\Delta \bar{x} = \sqrt{\frac{1}{\sum_{i=1}^N \frac{1}{\Delta x_i^2}}} \quad (4.2)$$

Two fiber mirror equipped fiber holders are necessary for the full functionality of the experiment, therefore testing was started with two fiber mirror candidates, called fiber1 and fiber2. As both fibers showed a finesse over 2600 they were both deemed sufficient for the experiment. The raw data used is given in App. A.1. The two fibers were also measured with the EOM-method, the results are visible in Fig. 4.7 and Fig. 4.8. With a finesse of 3973 for fiber1 and 3706 for fiber2 these results do not fit the FSR measurement well, with finesses of about 2661 and 2742. This could be the case because of some systematic error or scan non-linearity. The most reasonable option seems to be that the fits aren't ideal, especially the one in Fig. 4.7 seems to underestimate the dispersive part, but it is also a possibility, although unlikely, that these deviations occurred because of external vibrations that temporarily improved cavity alignment, because even though the theoretical finesse maximum of a $T_1 = 2000$ ppm on $T_2 = 10$ ppm fiber Fabry-Perot cavity lies around 3100, values higher than this are still possible because the coating process is not perfect and variations in the coatings reflectivity can occur. The theoretical maximum can be found for the case of low losses utilizing the formula for Lorentzian finesse [17], one then gets:¹

$$F = \frac{2\pi}{-\ln(R_1 \cdot R_2)} \approx \frac{2\pi}{-\ln((1 - T_1)(1 - T_2))} \approx 3122 \quad (4.3)$$

There was also a measurement conducted with fiber1 to determine the change of finesse that occurs when increasing the cavity length. The results of this measurement are shown in Fig. 4.9. The behavior is as expected except for an outlier at $54.5 \mu\text{m}$ (which could show such a deviation from the trend because of an external disruption for example). The constant value of the finesse drops off as the cavity mode starts to clip the spherical mirror area of the fiber mirror, as discussed in Sec. 2.1.2.

As stated before, fiber1 broke while assembling the main experiment and thus fiber2 took its place in the first fiber holder and was used for all further measurements, the second fiber holder remained empty

¹ The widely known approximate formula for a high reflectivity case can be found with $\ln(1 + x) \approx x$ for x close to 0, so $\frac{2\pi}{-\ln((1 - T_1)(1 - T_2))} = \frac{2\pi}{-(\ln(1 - T_1) + \ln(1 - T_2))} \approx \frac{2\pi}{T_1 + T_2}$

but will be fitted with an appropriate fiber mirror in the future.

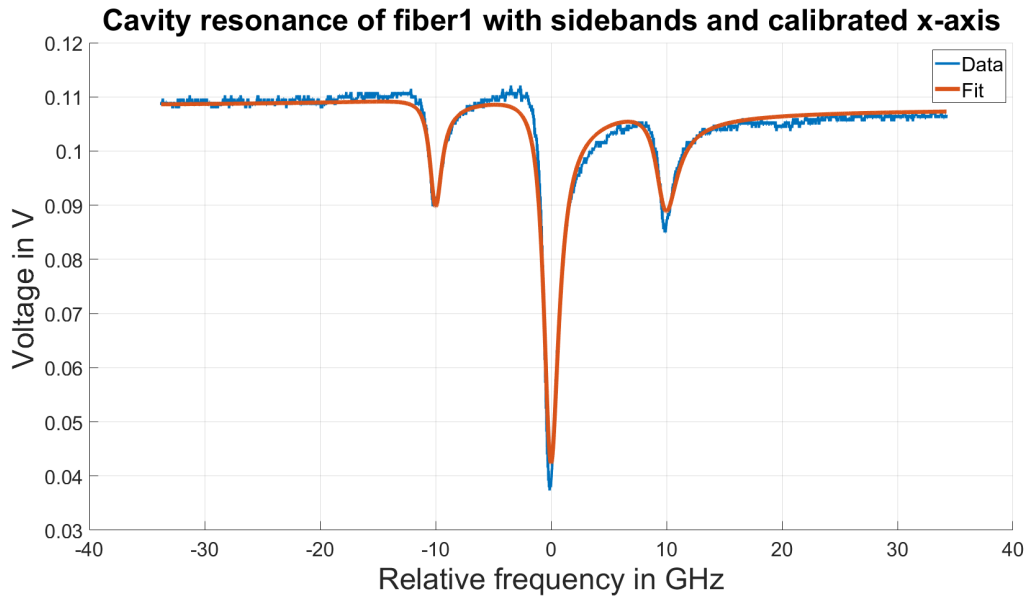


Figure 4.7: A cavity resonance of fiber1 with sidebands, created by the EOM, and with a calibrated x-axis. The fit estimates a finesse of 3973 ± 420 .

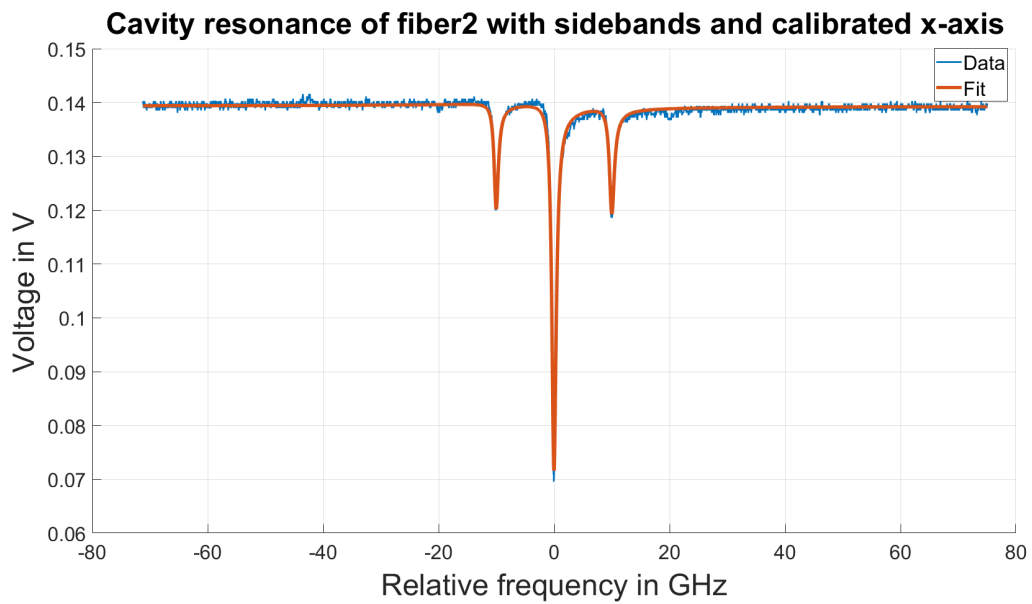


Figure 4.8: A cavity resonance of fiber2 with sidebands, created by the EOM, and with a calibrated x-axis. The fit estimates a finesse of 3706 ± 212 .

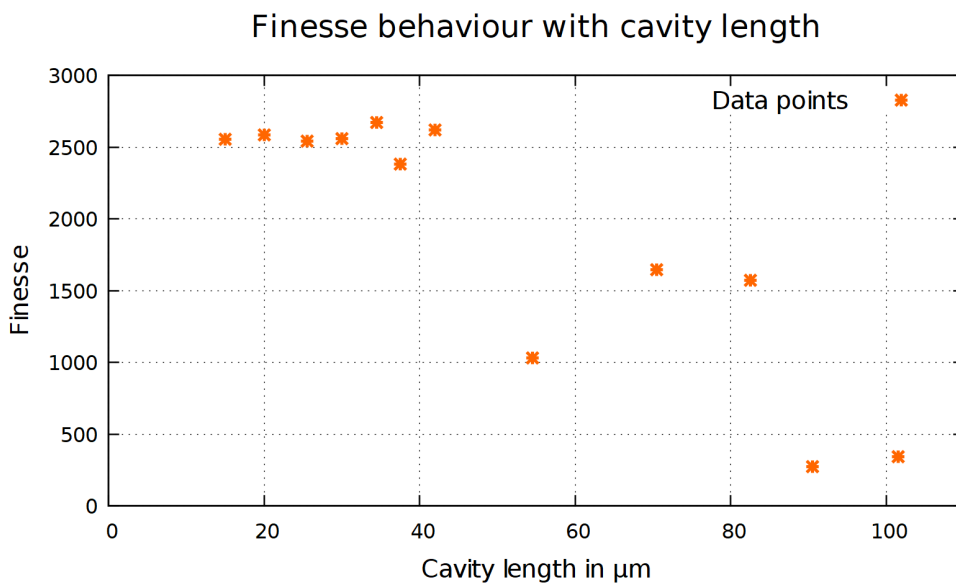


Figure 4.9: The results of the measurement series for the finesse behavior with changing cavity length.

4.1.2 Characterization of the Mirror Alignment

A central question for the realization of the fiber microscope is the alignability of the fiber mirror and substrate. As their common base is separated by several stages and adapters, an imprecise positioning or flexing of a component can possibly cause strong tilts rendering the realization of a high finesse cavity impossible. This consideration is especially important because the rotation stage does not directly provide any option for changing the mirrors tip and tilt orientation. If the performance achieved was not tolerable, it would be a possibility to switch the rotation stage for a vacuum-compatible adjustable mirror mount. But then the rotational degree of freedom in fiber positioning would be lost, which would be possible but disruptive when trying to position both fibers above fixed spots. This could for example pose a problem when trying to measure a complicated polymer structure, so if possible, this should be avoided. To investigate this problem a measurement series in which the mirror substrate is rotated between finesse measurements is conducted. If the substrate does not lie completely flat but is tilted, misalignment and thus finesse would significantly shift throughout the rotation. A second point of concern is whether the amount of slackness in the movement of the translation stages poses a problem. Consequently a measurement series in which the fiber is moved along the axis of stage 1 (here called x-direction) and the axis of stage 2 (here called y-direction) is conducted in the same way. If two linear positions of the stages lead to slightly different orthogonal positions due to wobbling, this would change the alignment and thus show up in the finesse.

One has to keep in mind that during these measurements fiber mirror and mirror substrate were not mechanically stabilized relative to each other yet (the actions described in Sec. 3.7 only happened after this). To partly compensate for that a Matlab[®] script was written to take ten measurements of the finesse in very short succession so that fast fluctuations can be averaged out. The ten data points for each measurement were then combined using the variance weighted arithmetic mean.

The Finesse was measured with the EOM method. The complete raw data is displayed in App. A.2. It is evident that the values fluctuate immensely. As stated already, values above the theoretical maximum are not necessarily unreasonable, because of possible manufacturing variations. Therefore these values are not excluded from the mean just because of this and consequently only measurements where the piezo scan range was highly nonlinear are not considered in the evaluation. An exemplary non-linear scan is shown in Fig. A.1. Non-linear scans occur close to an extremum point of the piezo scan waveform.

At first, the rotation measurement was conducted and the substrate was rotated in 45° steps. The results of the mean for every data point in dependence of angle are visible in Fig. 4.10. A clear systematic behavior in the finesse shift is visible, even though no direct sinusoidal conduct is evident. Possible explanations aside a not perfectly flat fitted mirror substrate, are a wobble or backlash of the rotation stage. Also an oscillation within the tolerance of the mounting system is possible. However, as the finesse is always above 1000 and most of the time close to or above 2000, the benefit in positioning flexibility that comes with using the rotation stage, outweighs the benefits in alignment capabilities one would have when utilizing an adjustable mirror mount.

After that the described measurement of the translation stage influence was conducted. The results are presented in Fig. 4.11. This measurement shows that the translation stages indeed seem to wobble while being moved, but without any obvious systematic behavior, which is good as it indicates that this process is statistically dominated. This means a repeated positioning at the same target position can improve occasionally occurring bad finesse values.

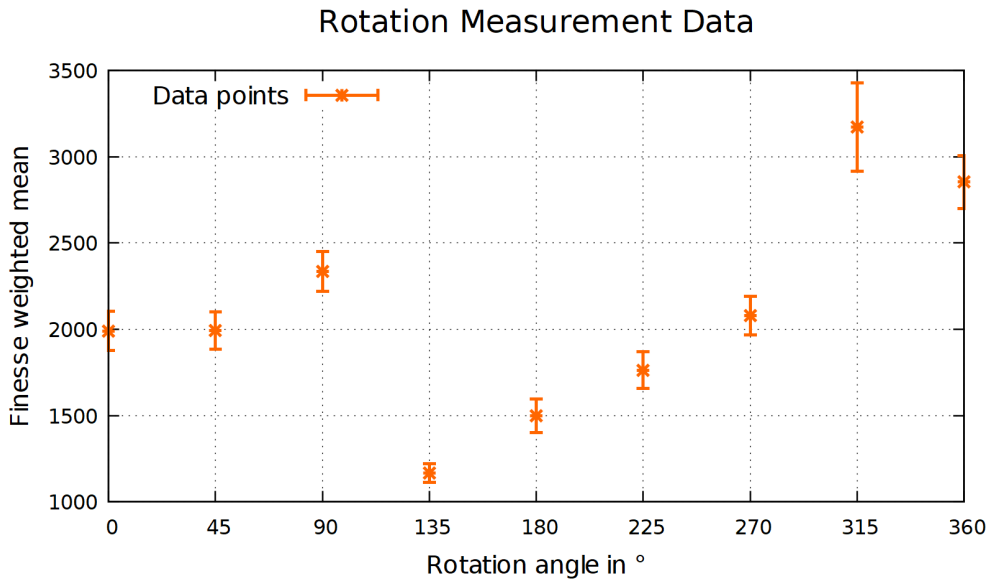


Figure 4.10: The weighted mean data points for the rotation measurement.

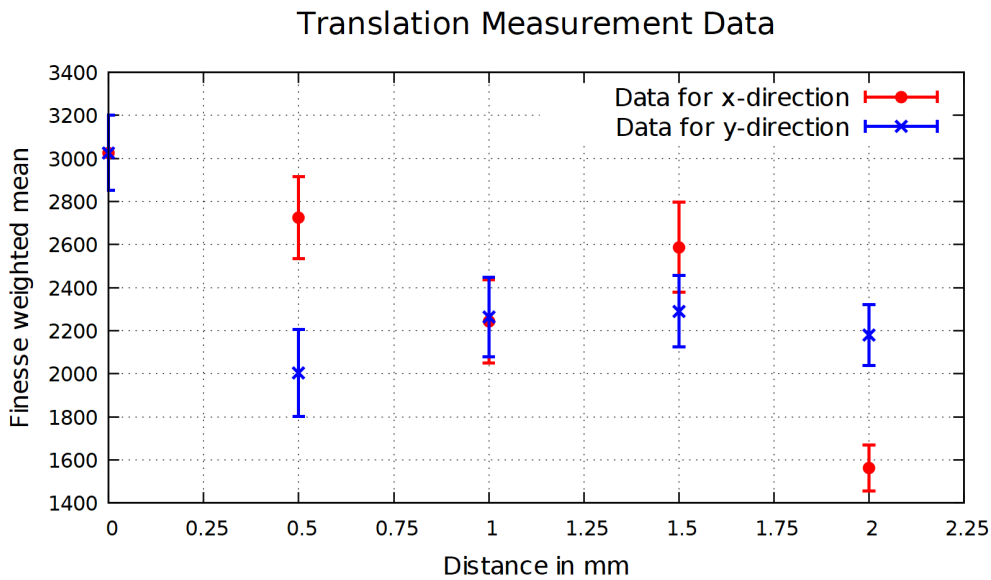


Figure 4.11: The weighted mean data points for the translation measurement in x- and y-direction.

4.2 Polymer Drum Resonance Measurement

Initially, it was tried to do a measurement of one of our polymer oscillator resonance frequencies before the efforts to stabilize the cavity, described in 3.7 were in place. However it was quickly found out that the setup was way too unstable to lock the cavity reliably. An image of attempting such a lock is visible in Fig. 4.12. Even these locking attempts were very difficult to achieve and highly unstable.

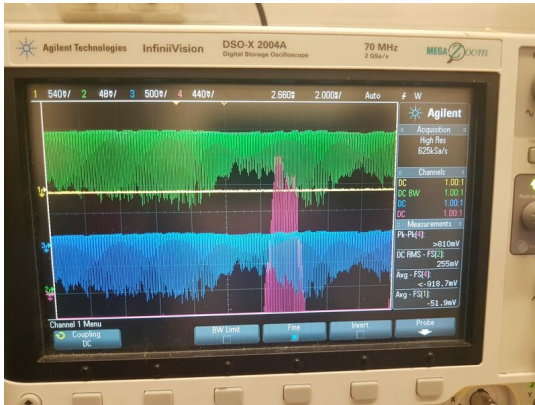


Figure 4.12: Oscilloscope image of a very unstable locking attempt, the stabilization signal to the piezo is visible in purple, the photo diode signal in green and the monitor signal in blue. The monitor signal is the one the lock box tries to stabilize internally and is here just a replica of the photo diode signal.

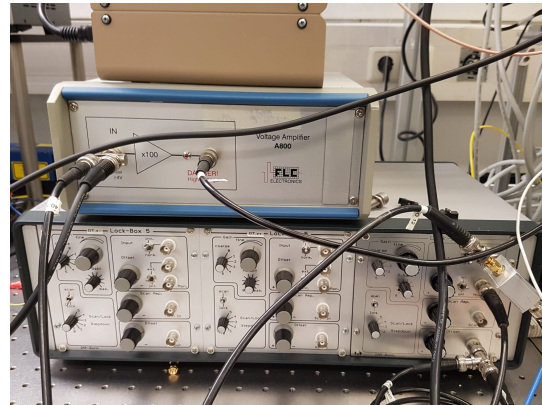


Figure 4.13: The lock-box used for locking the cavity with the piezo amplifier on top.

The PI-controller (Fig. 4.13) seemed to always over or under correct. After the modifications with the stabilization screw were in place, the stability was strongly improved and the cavity got lockable at the cost of a flexibility loss in the variation of the cavity length. After the lock had been achieved, a spectrum analyzer was attached to the photo diode signal. To protect the spectrum analyzer an attenuator, a high pass filter and a DC-Block were used. At first, a spectrum just on the plain mirror substrate was measured to rule any too disturbing electrical noise sources out. The result of this measurement is visible in Fig. 4.14, no significant noise source is visible (apart from the normal $\frac{1}{f}$ -noise, of course).

After positioning the fiber mirror above a drum, locking the cavity, and starting the measurement again, a resonance peak shows up on the spectrum analyzer (Fig. 4.16). After optimizing laser power and spectrum analyzer settings the fundamental mechanical resonance peak and a higher order mode are visible in the spectrum (Fig. 4.15).

The measurement (Fig. 4.15) yields a result for the mechanical resonance frequency of 1.472 MHz and a FWHM of 106.8 ± 2 kHz. This is in good agreement with a previous measurement of this polymer structure array that was conducted in 2020 by previous group members. It yielded a result for the resonance frequencies of around 1600 MHz. The deviation can be explained by aging and drying of the polymer material.

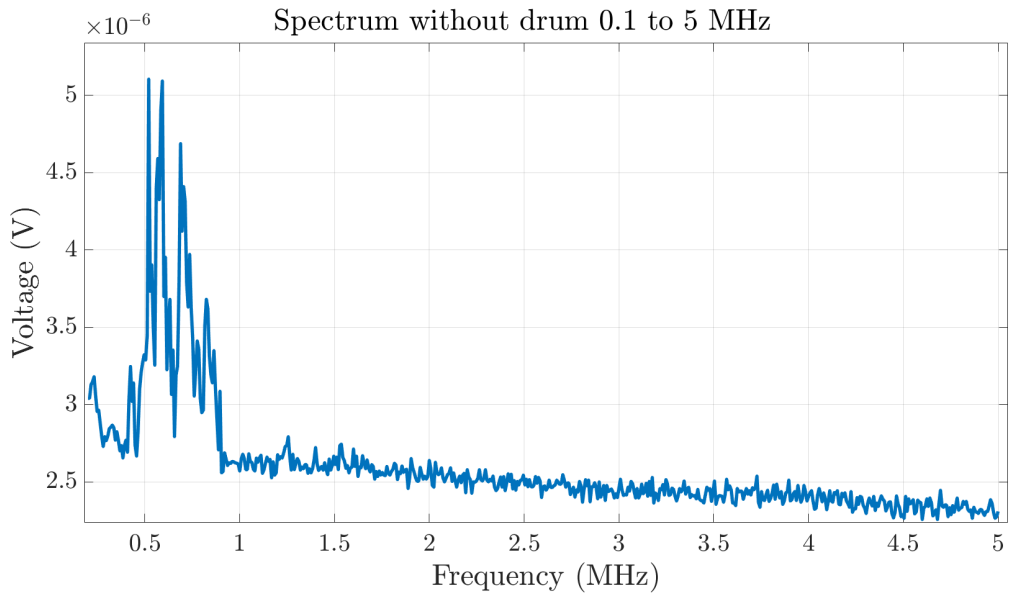


Figure 4.14: A spectrum of the cavity without a resonator.

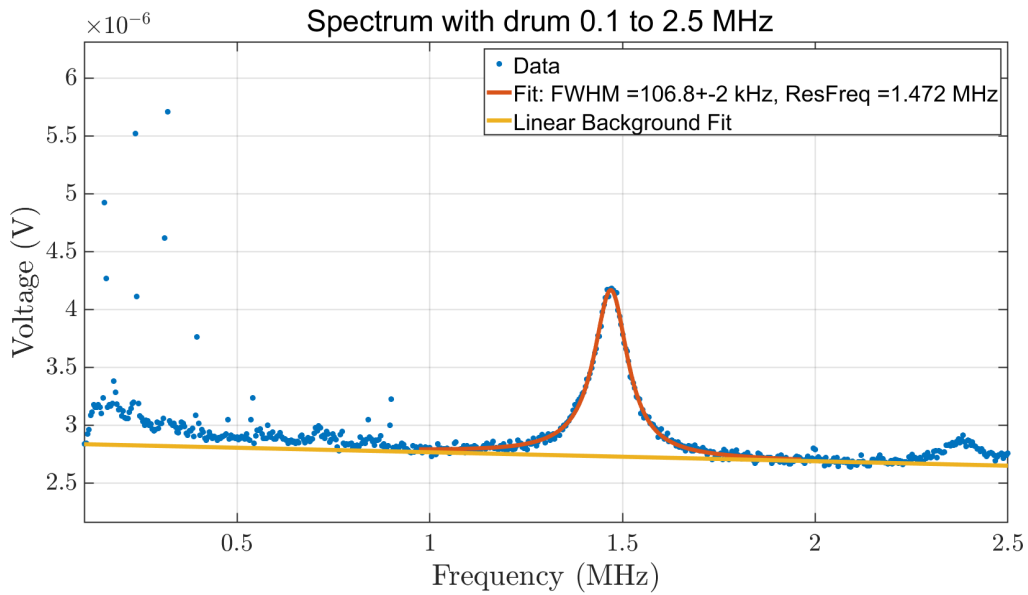


Figure 4.15: The optimized spectrum of the cavity with a mechanical resonator inside and improved x-scaling.

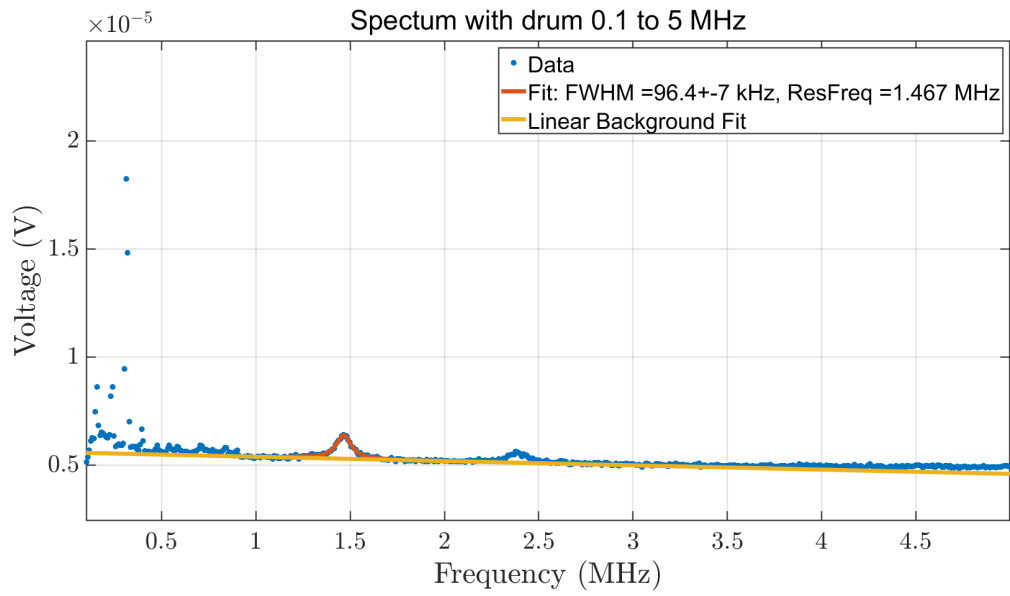


Figure 4.16: The initial spectrum of the cavity with a mechanical resonator inside.

Summary and Outlook

In this thesis it was shown that it is possible to build a vacuum fiber microscope, capable of reliably and precisely placing a fiber mirror above a mirror substrate to form scannable cavities in vacuum. Furthermore, it was shown how such a system can be constructed by utilizing electrically controlled vacuum compatible translation stages for fiber and mirror substrate positioning, a rotation stage for mirror substrate orientation control and a piezo for scanning the cavity length. As well as a fitting vacuum chamber, in addition to a 6-Way cross flange to handle all necessary feedthroughs and some further passive components. The elements were assembled in an outside protective structure and then lifted using a hoist to be positioned into the vacuum chamber. It was demonstrated that the system is, with slight modifications, capable of building stable single fiber Fabry-Perot cavities and that these cavities can be locked with sufficient stability to characterize integrated mechanical resonators. The fiber mirror used for the setup was selected by measuring its finesse in a simplified free space cavity setup. It was subsequently introduced into a fiber holder, consisting of an aluminum base with a glass ferrule to host the fiber and a piezo. This holder was then positioned on a translation stage inside the microscope structure that allows control over the cavity length. The fiber was fed through a Swagelok gas inlet, repurposed as a fiber-feedthrough and spliced to an optical patch cable for interfacing the laser. A measurement series regarding the finesse change on variation of the cavity length of the single fiber Fabry-Perot cavity (Sec. 4.1.1) reproduced the expected behavior of an almost constant finesse at first and a decrease due to clipping losses with increasing cavity length. The wobbling of the translation stages and alignment changes of the rotation stage on movement were also examined (Sec. 4.1.2) and both were determined to be largely unproblematic. A measurement of the mechanical resonance frequencies of a polymer oscillator was conducted (Sec. 4.2) and the resonance was observed at 1472 MHz. Furthermore, it was shown that the system is capable of reaching a vacuum pressure sufficient for optomechanical purposes (Fig. 3.57). The setup was planned and built with the capabilities to host a second fiber mirror in mind that can now be added in the immediate future by threading it into its holder and attaching it to the intended translation stage. With the second fiber mirror being implemented, the system will acquire the capability to operate two single fiber cavities above the mirror substrate at once, which will prove vital for interfacing advanced optomechanical polymer structures.

The experiment built in this thesis is now in a state where test measurements inside a vacuum can start, on success it will provide a platform for several future fiber cavity experiments, especially for those involving multimode optomechanical structures on a mirror substrate in vacuum. It is furthermore universally applicable for every experiment where structures on a mirror substrate have to

be investigated in a vacuum environment. The vacuum feature itself is crucial for research regarding low-loss optomechanical membrane structures in low-frequency ranges (below approximately 100MHz), to eliminate the dampening through air. Furthermore, the capabilities of the setup will keep increasing through the improvements proposed in Sec. 3.8. An additional mirror will allow us to observe the cavity length directly and an improved hoist system will make the transport of the setup between the vacuum chamber and the outer protective structure, used for maintenance and sample exchange, significantly easier. Improving the current primitive cavity stabilization mechanism that utilizes a screw, by instead using a linear extending stage, will make cavity length changes less complicated. Improving the control software will make the user experience more comfortable.

An especially interesting future project is to interface optomechanical oscillators on a mirror substrate electrically, for example by placing conductive tracks that form a capacitor with the drum itself on the mirror surface. This research could prove very useful in future developments of telecommunication technologies, as this can provide a possibility to modulate high-frequency electronic RF signals into light by just electrically driving the drum. The signals are then easily transmittable over large distances, this is especially useful for interfacing future quantum computers [18][19][20]. We also want to use the soon operational capabilities of the vacuum fiber microscope to place two fiber mirrors over the mirror substrate simultaneously to study complicated interconnected mechanical resonator structures. It is possible to actuate a part of the resonator assembly by a driving laser beam and then have this oscillation spread to neighboring regions of the oscillator assembly where they could be observed with the second fiber mirror. Between adjacent oscillators, one could then create a band gap, by slightly altering the resonant frequencies of the oscillators, or could prevent or encourage oscillation spread by utilizing the optical spring effect. This opens up rich possibilities in the construction of optomechanical circuits and could help to miniaturize optoacoustic wave filters [21] or to create optomechanical circulators or similar non-symmetric devices [22][23]. Other applications of these multi resonator optomechanical structures reach from enhancing already known optomechanical systems, where collective effects would improve coupling strength and dissipation [24][25], to investigations of quantum many-body dynamics [26][27][28]. Further possibilities lie in optomechanical accelerometers [29] or acoustic quantum computing[30].

Raw Data

1

A.1 Data of fiber candidates

FSR methode

Measurement	Finesse	Error
1	2697.32	10.79
2	2751.29	3.62
3	2778.20	4.41
4	2640.31	4.14
5	2643.24	5.20
6	2675.76	3.64
7	2523.79	2.35
8	2668.89	3.49
9	2768.26	3.10
10	2669.92	5.30
Weighted mean	2660.69	1.19

Table A.1: A series of measurements for the finesse of Fiber1, conducted with the FSR method.

Measurement	Finesse	Error
1	2396.08	5.45
2	2680.62	4.43
3	2816.32	4.08
4	2903.86	6.89
5	2200.05	3.94
6	2944.87	6.15
7	2859.67	4.49
8	2922.26	4.17
9	2851.84	5.15
10	2786.39	3.06
Weighted mean	2742.43	1.45

Table A.2: A series of measurements for the finesse of Fiber2, conducted with the FSR method.

¹ The Raw data used in this thesis can also be found in the fco vault under “\fcodata\FCO rawdata” in the folders “20220518”, “20220630” and “20220715”

Finesse with cavity length

Cavity length in μm	Finesse	Error Finesse
15	2555.60	3.55
20	2582.07	4.24
25.5	2542.83	2.40
30	2558.89	4.68
34.5	2669.92	5.30
37.5	2379.71	2.60
42	2619.88	2.31
54.5	1031.40	0.95
70.5	1646.63	2.24
82.5	1571.22	1.19
90.5	275.63	0.58
101.5	343.41	0.68

Table A.3: The finesse in dependence of cavity length measurement conducted with Fiber1.

A.2 Data: Characterization of the mirror alignment

A.2.1 Translation over mirror substrate

Measurement	Finesse	Error
1	3406	561
2	4473	717
3	3045	487
4	3582	573
5	2628	421
6	2212	354
7	3838	615
8	3616	579
9	3758	602
10	3749	605
Weighted mean	3026	175

Table A.4: The measured finesse values at the origin of the translation measurement with a 12 GHz signal at the EOM and a cavity length of $(37.5 \pm 6) \mu\text{m}$. The values 2 and 6 are excluded from the mean, as the piezo scan range was highly non-linear.

Measurement	Finesse	Error
1	2966	612
2	2621	541
3	2700	557
4	3597	742
5	2862	591
6	2161	446
7	2492	514
8	1073	223
9	2862	591
10	3256	679
Weighted mean	2725	190

Table A.5: The measured finesse values for a translation of $x + 0.5 \text{ mm}$ with a 12 GHz signal at the EOM and a cavity length of $(31.5 \pm 6.5) \mu\text{m}$. Value 8 is excluded from the mean, as the piezo scan range was highly non-linear.

Appendix A Raw Data

Measurement	Finesse	Error
1	3114	748
2	2150	516
3	2336	561
4	2043	491
5	2242	538
6	2141	514
7	2143	515
8	2205	530
9	3506	843
10	4424	1062
Weighted mean	2243	192

Table A.6: The measured finesse values for a translation of $x + 1$ mm with a 12 GHz signal at the EOM and a cavity length of (25 ± 6) μm . The values 1 and 10 are excluded from the mean, because their scan range was highly non-linear.

Measurement	Finesse	Error
1	2767	652
2	2948	694
3	4667	1098
4	2743	646
5	2582	608
6	3682	867
7	2566	604
8	1700	400
9	3260	767
10	3681	866
Weighted mean	2587	209

Table A.7: The measured finesse values for a translation of $x + 1.5$ mm with a 12 GHz signal at the EOM and a cavity length of (25.5 ± 6) μm . Value 3 is excluded from the mean, as the piezo scan range was highly non-linear.

Measurement	Finesse	Error
1	1568	336
2	1524	327
3	1524	327
4	1386	297
5	1876	402
6	1641	352
7	1397	300
8	1718	369
9	1577	338
10	1649	354
Weighted mean	1563	106

Table A.8: The measured finesse values for a translation of $x + 2$ mm with a 12 GHz signal at the EOM and a cavity length of (28 ± 6) μm .

Measurement	Finesse	Error
1	1745	553
2	2080	660
3	2410	764
4	2332	740
5	1783	566
6	1627	516
7	2097	665
8	2470	783
9	2084	661
10	2160	685
Weighted mean	2004	203

Table A.9: The measured finesse values for a translation of $y + 0.5$ mm with a 12 GHz signal at the EOM and a cavity length of (20.5 ± 6.5) μm .

Appendix A Raw Data

Measurement	Finesse	Error
1	1995	508
2	2319	590
3	2180	555
4	2004	510
5	1997	508
6	2351	598
7	2904	739
8	3420	871
9	2129	542
10	2570	654
Weighted mean	2264	184

Table A.10: The measured finesse values for a translation of $y + 1$ mm with a 12 GHz signal at the EOM and a cavity length of (27.5 ± 7) μm .

Measurement	Finesse	Error
1	2701	548
2	8212	1669
3	2356	478
4	2148	436
5	2649	538
6	2815	571
7	2221	451
8	2733	555
9	2361	479
10	1813	368
Weighted mean	2291	166

Table A.11: The measured finesse values for a translation of $y + 1.5$ mm with a 12 GHz signal at the EOM and a cavity length of (34.5 ± 7) μm . The values 2 and 6 are excluded from the mean, because their scan was highly non-linear.

Measurement	Finesse	Error
1	2941	588
2	2247	450
3	1967	394
4	2110	422
5	2548	510
6	3892	779
7	3000	600
8	2993	599
9	1775	355
10	1561	312
Weighted mean	2180	143

Table A.12: The measured finesse values for a translation of $y + 2$ mm with a 12 GHz signal at the EOM and a cavity length of (35 ± 7) μm .

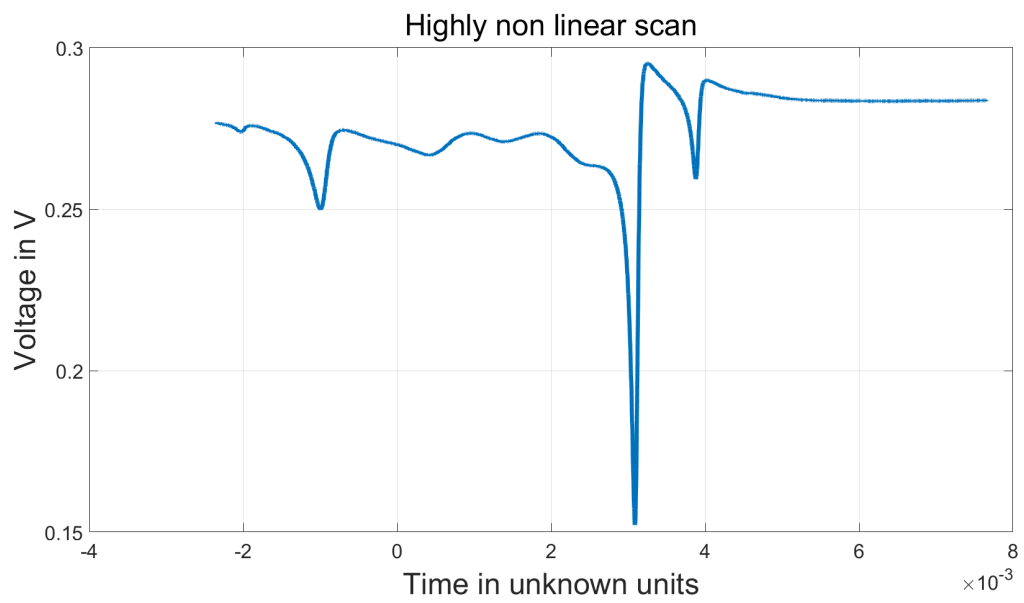


Figure A.1: A cavity resonance with sidebands and a highly non-linear piezo scan.

A.2.2 Rotation over mirror substrate

Measurement	Finesse	Error
1	2251	388
2	2375	409
3	2268	391
4	1953	337
5	1854	320
6	1879	324
7	1715	296
8	2265	391
9	1906	328
0	2089	360
Weighted mean	1991	115

Table A.13: The measured finesse values for a 0° rotated mirror with a 12 GHz signal at the EOM and a cavity length of $(46.5 \pm 8) \mu\text{m}$. Value 1 is excluded from the mean, as the piezo scan range was highly non-linear.

Measurement	Finesse	Error
1	1854	316
2	2602	444
3	2287	390
4	2166	369
5	2809	479
6	2075	354
7	2088	356
8	2130	363
9	1996	340
10	1382	236
Weighted mean	1992	110

Table A.14: The measured finesse values for a 45° rotated mirror with a 12 GHz signal at the EOM and a cavity length of $(47 \pm 8) \mu\text{m}$.

Measurement	Finesse	Error
1	2038	284
2	756	106
3	2300	320
4	2113	294
5	2493	348
6	2492	347
7	2623	365
8	812	113
9	2101	293
10	3282	458
Weighted mean	2335	116

Table A.15: The measured finesse values for a 90° rotated mirror with a 12 GHz signal at the EOM and a cavity length of $(54 \pm 7.5) \mu\text{m}$. The values 2 and 8 are excluded from the mean, as their piezo scan range was highly non-linear.

Measurement	Finesse	Error
1	1524	203
2	1090	145
3	1239	165
4	1131	150
5	944	125
6	1675	223
7	493	66
8	985	131
9	1281	170
10	1307	174
Weighted mean	1167	53

Table A.16: The measured finesse values for a 135° rotated mirror with a 12 GHz signal at the EOM and a cavity length of $(49 \pm 6.5) \mu\text{m}$. Value 7 is excluded from the mean, as the piezo scan range was highly non-linear.

Appendix A Raw Data

Measurement	Finesse	Error
1	2174	441
2	1337	272
3	1439	292
4	1119	227
5	1842	374
6	1779	362
7	1747	355
8	1369	278
9	1638	333
10	1552	315
Weighted mean	1498	98

Table A.17: The measured finesse values for a 180° rotated mirror with a 12 GHz signal at the EOM and a cavity length of (34.5 ± 7) μm .

Measurement	Finesse	Error
1	1790	298
2	2178	363
3	1677	280
4	3718	623
5	1678	280
6	1877	313
7	1421	237
8	2110	352
9	3023	504
10	1849	308
Weighted mean	1764	105

Table A.18: The measured finesse values for a 225° rotated mirror with a 12 GHz signal at the EOM and a cavity length of (42 ± 7) μm . The values 4 and 9 are excluded from the mean, as their piezo scan range was highly non-linear.

Measurement	Finesse	Error
1	1691	282
2	2808	468
3	2632	439
4	2467	411
5	2055	343
6	1774	296
7	2111	352
8	1898	317
9	2962	494
10	1881	314
Weighted mean	2079	111

Table A.19: The measured finesse values for a 270° rotated mirror with a 12 GHz signal at the EOM and a cavity length of (42 ± 7) μm .

Measurement	Finesse	Error
1	2564	615
2	3996	959
3	5461	1311
4	3270	787
5	2982	716
6	3020	725
7	3146	755
8	3082	740
9	3619	869
10	3864	928
Weighted mean	3170	256

Table A.20: The measured finesse values for a 315° rotated mirror with a 12 GHz signal at the EOM and a cavity length of (25 ± 6) μm . Value 3 is excluded from the mean, as the piezo scan range was highly non-linear.

Measurement	Finesse	Error
1	2871	459
2	3802	609
3	4125	660
4	3181	509
5	3126	500
6	3146	503
7	2784	446
8	2468	395
9	2428	389
10	2755	441
Weighted mean	2853	153

Table A.21: The measured finesse values for a 360° rotated mirror with a 12 GHz signal at the EOM and a cavity length of $(37.5 \pm 6) \mu\text{m}$. Value 3 is excluded from the mean, as the piezo scan range was highly non-linear.

Bibliography

- [1] K. Iizuka, “History of Optics,” *Engineering Optics*, Cham: Springer International Publishing, 2019 1, ISBN: 978-3-319-69251-7, URL: https://doi.org/10.1007/978-3-319-69251-7_1 (cit. on p. 1).
- [2] J. Kepler, *De Cometis Libelli Tres*, 1619 (cit. on p. 1).
- [3] *Cavity Optomechanics: Brief introduction*, URL: <https://mpl.mpg.de/divisions/marquardt-division/research/in-depth-cavity-optomechanics/> (cit. on p. 1).
- [4] M. Mader, J. Reichel, T. W. Hänsch, and D. Hunger, *A scanning cavity microscope*, *nature communications* (2015), URL: <https://www.nature.com/articles/ncomms8249> (cit. on p. 1).
- [5] D. Meschede, *Optik, Licht und Laser*, 3rd ed., Vieweg+Teubner, 2008 (cit. on p. 2).
- [6] A. Yariv and P. Yeh, *Photonics*, 6th ed., Oxford University Press, 2007 (cit. on pp. 4, 32).
- [7] R. Kitamura, L. Pilon, and M. Jonasz, *Optical constants of silica glass from extreme ultraviolet to far infrared at near room temperature*, *Appl. Opt.* **46** (2007) 8118, URL: <http://opg.optica.org/ao/abstract.cfm?URI=ao-46-33-8118> (cit. on p. 4).
- [8] L. Tenbrake, *Fiber Cavity Optomechanics with Polymer Membranes*, MA thesis: Institut für angewandte Physik Universität Bonn, 2021 (cit. on pp. 4–6, 8).
- [9] *RefractiveIndex.info, Ta2O5, Rodriguez-de Marcos et al. 2016*, URL: https://refractiveindex.info/?shelf=main&book=Ta2O5&page=Rodriguez-de_Marcos (cit. on p. 4).
- [10] *RefractiveIndex.info, SiO2, Rodriguez-de Marcos et al. 2016: Thin film*, URL: https://refractiveindex.info/?shelf=main&book=SiO2&page=Rodriguez-de_Marcos (cit. on p. 4).
- [11] J. C. Gallego, *Strong Coupling between Small Atomic Ensembles and an Open Fiber Cavity*, (2017), URL: <http://quantum-technologies.iap.uni-bonn.de/de/group-members/164-jose-c-gallego-fernandez.html> (cit. on pp. 4, 5).
- [12] M. Aspelmeyer, T. J. Kippenberg, and F. Marquardt, “Introduction,” *Cavity Optomechanics: Nano- and Micromechanical Resonators Interacting with Light*, ed. by M. Aspelmeyer, T. J. Kippenberg, and F. Marquardt, Berlin, Heidelberg: Springer Berlin Heidelberg, 2014 1, ISBN: 978-3-642-55312-7, URL: https://doi.org/10.1007/978-3-642-55312-7_1 (cit. on p. 5).

-
- [13] M. Aspelmeyer, T. J. Kippenberg, and F. Marquardt, *Cavity optomechanics*, *Rev. Mod. Phys.* **86** (4 2014) 1391,
URL: <https://link.aps.org/doi/10.1103/RevModPhys.86.1391> (cit. on p. 5).
- [14] Z. Fang, H. Cai, G. Chen, and R. Qu, “Frequency Stabilization of Semiconductor Lasers,” *Single Frequency Semiconductor Lasers*, Singapore: Springer Singapore, 2017 167,
ISBN: 978-981-10-5257-6, URL: https://doi.org/10.1007/978-981-10-5257-6_6
(cit. on p. 6).
- [15] C. Saavedra, D. Pandey, W. Alt, H. Pfeifer, and D. Meschede,
Tunable fiber Fabry-Perot cavities with high passive stability, *Opt. Express* **29** (2021) 974,
URL: <http://opg.optica.org/oe/abstract.cfm?URI=oe-29-2-974> (cit. on p. 8).
- [16] *M-110 • M-111 • M-112 V6 Vacuum-Compatible Compact Linear Stage*,
URL: <https://www.physikinstrumente.com/en/products/linear-stages/stages-with-stepper-dc-brushless-dc-bl-dc-motors/m-110-m-111-m-112-v6-compact-linear-stage-suitable-for-vacuum-412418485/> (cit. on p. 8).
- [17] N. Ismail, C. C. Kores, D. Geskus, and M. Pollnau,
Fabry-Perot resonator: spectral line shapes, generic and related Airy distributions, linewidths, finesse, and performance at low or frequency-dependent reflectivity,
Opt. Express **24** (2016) 16366,
URL: <http://opg.optica.org/oe/abstract.cfm?URI=oe-24-15-16366> (cit. on p. 35).
- [18] R. W. Andrews et al., *Bidirectional and efficient conversion between microwave and optical light*,
Nature Physics **10** (2014), URL: <https://doi.org/10.1038/nphys2911> (cit. on p. 44).
- [19] X. Han, W. Fu, C.-L. Zou, L. Jiang, and H. X. Tang,
Microwave-optical quantum frequency conversion, *Optica* **8** (2021) 1050,
URL: <http://opg.optica.org/optica/abstract.cfm?URI=optica-8-8-1050>
(cit. on p. 44).
- [20] M. Mirhosseini, A. Sipahigil, M. Kalaei, and O. Painter,
Superconducting qubit to optical photon transduction, *Nature* **588** (2020),
URL: <https://doi.org/10.1038/s41586-020-3038-6> (cit. on p. 44).
- [21] T. Vasileiadis et al., *Progress and perspectives on phononic crystals*,
Journal of Applied Physics **129** (2021) 160901,
eprint: <https://doi.org/10.1063/5.0042337>,
URL: <https://doi.org/10.1063/5.0042337> (cit. on p. 44).
- [22] S. Barzanjeh et al., *Mechanical on-chip microwave circulator*, *Nature Communications* **8** (2017),
URL: <https://doi.org/10.1038/s41467-017-01304-x> (cit. on p. 44).
- [23] K. Fang et al., *Generalized non-reciprocity in an optomechanical circuit via synthetic magnetism and reservoir engineering*, *Nature Phys* **13** (2017),
URL: <https://doi.org/10.1038/nphys4009> (cit. on p. 44).
- [24] A. Xuereb, C. Genes, and A. Dantan,
Strong Coupling and Long-Range Collective Interactions in Optomechanical Arrays,
Phys. Rev. Lett. **109** (22 2012) 223601,
URL: <https://link.aps.org/doi/10.1103/PhysRevLett.109.223601> (cit. on p. 44).

- [25] M. H. J. de Jong, J. Li, C. Gärtner, R. A. Norte, and S. Gröblacher, *Coherent mechanical noise cancellation and cooperativity competition in optomechanical arrays*, *Optica* **9** (2022) 170, URL: <http://opg.optica.org/optica/abstract.cfm?URI=optica-9-2-170> (cit. on p. 44).
- [26] M. Ludwig and F. Marquardt, *Quantum Many-Body Dynamics in Optomechanical Arrays*, *Phys. Rev. Lett.* **111** (7 2013) 073603, URL: <https://link.aps.org/doi/10.1103/PhysRevLett.111.073603> (cit. on p. 44).
- [27] M. Schmidt, V. Peano, and F. Marquardt, *Optomechanical Metamaterials: Dirac polaritons, Gauge fields, and Instabilities*, 2013, URL: <https://arxiv.org/abs/1311.7095> (cit. on p. 44).
- [28] J. P. Mathew, J. del Pino, and E. Verhagen, *Synthetic gauge fields for phonon transport in a nano-optomechanical system*, *Nature Nanotechnology* **15** (2020), URL: <https://doi.org/10.1038/s41565-019-0630-8> (cit. on p. 44).
- [29] A. G. Krause, M. Winger, T. D. Blasius, Q. Lin, and O. Painter, *A high-resolution microchip optomechanical accelerometer*, *Nature Photonics* **6** (2012), URL: <https://doi.org/10.1038/nphoton.2012.245> (cit. on p. 44).
- [30] A. Zivari et al., *On-chip distribution of quantum information using traveling phonons*, 2022, URL: <https://arxiv.org/abs/2204.05066> (cit. on p. 44).

List of Figures

2.1	Qualitative plot of the transmission spectrum into the cavity for a lower (red) and a higher finesse (blue).	3
2.2	The fiber shooting setup.	4
2.3	The Nanoscribe 3D-Printing system.	4
2.4	Taken from [8, p. 35]. Left: Map of the coupling, L_2 is the length of the mechanical oscillators feet, n is the index of refraction of the drum material and d is the drum thickness. Right: Four particular interesting spots of the map are selected, points of very high coupling in the forwards and backwards direction (1 and 2) and points of low coupling (3 and 4). The intensity distribution around the drum (grey) is shown.	6
3.1	A sketch of the monolithic fiber Fabry-Perot cavities [8] (adapted from [15]). The ferrule is visible in blue and glued to the piezo below, the fibers are threaded into the ferrule and form a cavity at its center. The fibers are glued into place at the outside pieces of the ferrule but free to move in the inside section thus the cavity gets scannable when applying a piezo voltage.	8
3.2	Inventor model of the inner structure.	9
3.3	The stage numbering convention.	9
3.4	The basic outer support and protection structure. One can see the aluminum scaffolding on the sides, the 6-Way cross at the top and the aluminum breadboard at the bottom.	10
3.5	The basic outer support and protection structure with the inner frame for stage attachment partially assembled.	10
3.6	The stages 2 and 4 hooked to their controller for first interface testing.	11
3.7	One of the translation stage controllers.	11
3.8	The MicroMove [®] interface to add the stage daisy chain.	12
3.9	The custom translation stage feedthroughs.	12
3.10	The whole translation stage controller stack in the daisy chain configuration. The individual controllers were connected to each other and one had to input their binary address in the daisy chain by switching their “Addr.”-buttons.	13
3.11	The inner aluminum structure with the first translation stage that will control the left fiber.	13
3.12	The first three translation stages, which are the ones needed for the simplified one fiber setup, were assembled and attached to the main aluminum frame. The control units are visible in the background.	14
3.13	Complete assembly of the basic setups inner structure, now with the rotation stage attached.	14
3.14	The rotation stage that will hold the mirror substrate for the experiment.	15
3.15	Cut rotation stage cable stripped of isolation and with twisted outer conductor.	15

List of Figures

3.16	The 6-Way cross in its first testing configuration. The left flange allows interface to the translation stages 1-3 and the right one carries the electrical feedthrough for the rotation stage. Flanges for fiber feedthrough, piezo control and interface of stage 4 and 5 are still missing.	15
3.17	The top 6-Way cross in its final configuration, the connection to the electrical feedthrough of the rotation stage was made more permanent and a cap was added for protecting the fiber during transport (Sec. 3.6.2).	15
3.18	As stage 5 had to be mounted to stage 4, an aluminum connection block was necessary, the through holes of stage 5 were used with brass screws to interface it.	16
3.19	The feedthrough flange for stage 4 and stage 5.	17
3.20	A Swagelok gas inlet repurposed as a fiber feedthrough.	17
3.21	The copper rod feedthrough for the piezos, connected to Kapton [®] coated copper cables using CuBe-connectors.	17
3.22	The 6-Way cross with the cables for stages 4 and 5 hanging out.	17
3.23	The “Fujikura ArcMaster FSM-100P+” splicer.	18
3.24	A fiber placed in an Fe(III)Cl solution.	18
3.25	Fiber mirror and elongation are spliced together in the Fujikura splicer. The two fibers intended for splicing were clamped into the dedicated holders, visible on the sides, and the two central electrodes will provide an arc that fuses the fibers together.	18
3.26	The tools necessary to strip an optical patch cable of its isolation, special pliers for the outside isolation (right) and a dedicated stripper for the inside one (left).	18
3.27	The fully functional control interface window with a live view of the mirror substrate, and a console printing a message about every action conducted, on the right, and control buttons for repositioning, servo switching, and controller disconnection, as well as displays for position monitoring, on the left.	19
3.28	The two-component silver glue used.	20
3.29	The UV-glue used.	20
3.30	A microscope image of the isolation, the piezo and the piezo wires on the holder.	20
3.31	The ferrule glued in the fiber holder base with the fiber mirror threaded in. One sees the back end of the ferrule, further on the top right the piezo is located and further down left the fiber mirror tip peaks out the ferrule for a few millimeters.	20
3.32	The basic mirror testing setup, consisting just of a fiber mirror, attached to a manual translation stage, and a mirror substrate.	21
3.33	Deep cavity dips imply a strong coupling and give first indications that the fiber is working correctly.	21
3.34	The fiber stockpile holder in which the fibers are placed when they arrive from the coating company.	22
3.35	The dental drill.	22
3.36	The fiber threading (left) and basic mirror testing setup (right), a UV-lamp is placed above the fiber holder for curing of the UV-glue after threading.	22
3.37	The fiber holder while the ferrule is threaded through.	22
3.38	The Macor [®] Ceramic plates used in building the fiber holders for piezo isolation.	23
3.39	The dental drill is being used for removing excess material.	23
3.40	The finished first fiber holder, with the ferrule at its tip and the piezo positioned further to the right. The fiber is not introduced yet.	23

List of Figures

3.41	The second fiber holder that will place the second fiber above the mirror substrate as soon as the experimental setup is completed. Piezo and ferrule are visible on the right.	23
3.42	The UV-glue as it was applied to the piezo to fixate fiber1.	23
3.43	The UV-glue while curing under the UV-lamp.	23
3.44	A sketch of the vacuum system structure.	24
3.45	A monolithic fiber cavity in the old vacuum setup, which is now the secondary experiment chamber. The monolithic fiber cavity is placed on top of a Teflon platform and fixated by a clamping Teflon piece over the piezo interfacing cables.	25
3.46	The first configuration of the vacuum setup during the first pump down test. The controller for the ion pump is visible on the left.	25
3.47	The connection between the DN 100 T-piece and the main experiment chamber, with the valve separating the experiment chamber and the rest of the vacuum setup.	25
3.48	A pressure reading of $5.07 \cdot 10^{-7}$ mbar on the turbo pump after a few hours of pumping, but without the experiment introduced yet.	25
3.49	View onto the whole vacuum setup, with the experiment chamber attached.	26
3.50	The whole experimental setup up to this point, the vacuum chamber now has a blind flange on top.	26
3.51	Sight into the main experiment chamber, before the view port is screwed on.	26
3.52	The rail and hoist used for inner structure transportation.	27
3.53	Some polymer drums as seen through the view port with an USB-microscope.	27
3.54	The inner setup hovering over the lowered aluminum plate of the outer protective structure.	28
3.55	The experimental setup was moved to the vacuum chamber.	28
3.56	The inner setup was lowered into the vacuum chamber.	29
3.57	A pressure reading after two weeks of pumping with the turbopump of $2.6 \cdot 10^{-6}$ mbar.	29
3.58	The mirror substrate as seen from the viewport on the bottom of the experiment chamber.	29
3.59	The inner structure connected to the hoist.	29
3.60	The L-piece in “Inventor”.	30
3.61	The L-piece with a threaded M3 hole for holding the stabilization screw and two M2 through holes for connection to the fiber holder on stage 3.	30
3.62	The L-piece with screw and UV-glue at its tip.	31
3.63	The L-piece attached to its desired position on the first fiber holder.	31
4.1	The beam splitter used in the experiment.	33
4.2	An image of the photo diode used in the experiment.	33
4.3	An image of the electro-optical modulator.	33
4.4	The function generator that drives the EOM.	33
4.5	The control interface for the waveform generator that feeds the EOM.	34
4.6	A microscope image of a fiber in the basic mirror testing setup.	34
4.7	A cavity resonance of fiber1 with sidebands, created by the EOM, and with a calibrated x-axis. The fit estimates a finesse of 3973 ± 420 .	36
4.8	A cavity resonance of fiber2 with sidebands, created by the EOM, and with a calibrated x-axis. The fit estimates a finesse of 3706 ± 212 .	36
4.9	The results of the measurement series for the finesse behavior with changing cavity length.	37
4.10	The weighted mean data points for the rotation measurement.	39
4.11	The weighted mean data points for the translation measurement in x- and y-direction.	39

List of Figures

4.12	Oscilloscope image of a very unstable locking attempt, the stabilization signal to the piezo is visible in purple, the photo diode signal in green and the monitor signal in blue. The monitor signal is the one the lock box tries to stabilize internally and is here just a replica of the photo diode signal.	40
4.13	The lock-box used for locking the cavity with the piezo amplifier on top.	40
4.14	A spectrum of the cavity without a resonator.	41
4.15	The optimized spectrum of the cavity with a mechanical resonator inside and improved x-scaling.	41
4.16	The initial spectrum of the cavity with a mechanical resonator inside.	42
A.1	A cavity resonance with sidebands and a highly non-linear piezo scan.	49

List of Tables

A.1	A series of measurements for the finesse of Fiber1, conducted with the FSR method.	45
A.2	A series of measurements for the finesse of Fiber2, conducted with the FSR method.	45
A.3	The finesse in dependence of cavity length measurement conducted with Fiber1.	46
A.4	The measured finesse values at the origin of the translation measurement with a 12 GHz signal at the EOM and a cavity length of $(37.5 \pm 6) \mu\text{m}$. The values 2 and 6 are excluded from the mean, as the piezo scan range was highly non-linear.	46
A.5	The measured finesse values for a translation of $x + 0.5$ mm with a 12 GHz signal at the EOM and a cavity length of $(31.5 \pm 6.5) \mu\text{m}$. Value 8 is excluded from the mean, as the piezo scan range was highly non-linear.	46
A.6	The measured finesse values for a translation of $x + 1$ mm with a 12 GHz signal at the EOM and a cavity length of $(25 \pm 6) \mu\text{m}$. The values 1 and 10 are excluded from the mean, because their scan range was highly non-linear.	47
A.7	The measured finesse values for a translation of $x + 1.5$ mm with a 12 GHz signal at the EOM and a cavity length of $(25.5 \pm 6) \mu\text{m}$. Value 3 is excluded from the mean, as the piezo scan range was highly non-linear.	47
A.8	The measured finesse values for a translation of $x + 2$ mm with a 12 GHz signal at the EOM and a cavity length of $(28 \pm 6) \mu\text{m}$	47
A.9	The measured finesse values for a translation of $y + 0.5$ mm with a 12 GHz signal at the EOM and a cavity length of $(20.5 \pm 6.5) \mu\text{m}$	47
A.10	The measured finesse values for a translation of $y + 1$ mm with a 12 GHz signal at the EOM and a cavity length of $(27.5 \pm 7) \mu\text{m}$	48
A.11	The measured finesse values for a translation of $y + 1.5$ mm with a 12 GHz signal at the EOM and a cavity length of $(34.5 \pm 7) \mu\text{m}$. The values 2 and 6 are excluded from the mean, because their scan was highly non-linear.	48
A.12	The measured finesse values for a translation of $y + 2$ mm with a 12 GHz signal at the EOM and a cavity length of $(35 \pm 7) \mu\text{m}$	48
A.13	The measured finesse values for a 0° rotated mirror with a 12 GHz signal at the EOM and a cavity length of $(46.5 \pm 8) \mu\text{m}$. Value 1 is excluded from the mean, as the piezo scan range was highly non-linear.	50
A.14	The measured finesse values for a 45° rotated mirror with a 12 GHz signal at the EOM and a cavity length of $(47 \pm 8) \mu\text{m}$	50
A.15	The measured finesse values for a 90° rotated mirror with a 12 GHz signal at the EOM and a cavity length of $(54 \pm 7.5) \mu\text{m}$. The values 2 and 8 are excluded from the mean, as their piezo scan range was highly non-linear.	50

List of Tables

A.16	The measured finesse values for a 135° rotated mirror with a 12 GHz signal at the EOM and a cavity length of $(49 \pm 6.5) \mu\text{m}$. Value 7 is excluded from the mean, as the piezo scan range was highly non-linear.	50
A.17	The measured finesse values for a 180° rotated mirror with a 12 GHz signal at the EOM and a cavity length of $(34.5 \pm 7) \mu\text{m}$	51
A.18	The measured finesse values for a 225° rotated mirror with a 12 GHz signal at the EOM and a cavity length of $(42 \pm 7) \mu\text{m}$. The values 4 and 9 are excluded from the mean, as their piezo scan range was highly non-linear.	51
A.19	The measured finesse values for a 270° rotated mirror with a 12 GHz signal at the EOM and a cavity length of $(42 \pm 7) \mu\text{m}$	51
A.20	The measured finesse values for a 315° rotated mirror with a 12 GHz signal at the EOM and a cavity length of $(25 \pm 6) \mu\text{m}$. Value 3 is excluded from the mean, as the piezo scan range was highly non-linear.	51
A.21	The measured finesse values for a 360° rotated mirror with a 12 GHz signal at the EOM and a cavity length of $(37.5 \pm 6) \mu\text{m}$. Value 3 is excluded from the mean, as the piezo scan range was highly non-linear.	52